Sudan University of Sciences and Technology

College of Graduate Studies

Quantitative Evaluation of Breast Lesion Based on Ultrasound Elastography

التقييم الكمي لكتلة الثدي الصلبة اعتماداً على مرونة الأنسجة بالموجات فوق الصوتية

A Dissertation Submitted for Partial Fulfillment of Requirement for Master Degree in Biomedical Engineering

Submitted by:

Hiba Mohamed Elfatih Ahmed Mohamed Doleib

Supervisor:

Dr. Musab Alkhair Salah

March, 2018

الآية

قَالَ اللهُ تَعَالَى:

(قُلِ اللَّهُمَّ مَلِكَ الْمُلْكِ تُؤْتِي الْمُلْكَ مَن تَشَاءُ وَتَنزِعُ الْمُلْكَ مِمَّن تَشَاءُ وَتُعِزُّ مَن تَشَاءُ وَتُذِلُّ مَن تَشَاءُ بِيَدِكَ الْخَيْرُ إِنَّكَ عَلَى كُلِّ شَيْءٍ قَدِيرٌ)

صَدَقَ اللهُ العَظِيم

(آلِ عِمرَانَ:25)

Acknowledgement

First and foremost, I am very grateful to those who provided me with professional assistance during the writing of my dissertation.

I extend my sincere gratitude to my supervisor, **Dr. Musab Alkhair Salah** for the continuous support of my MSc study and research, for his patience, motivation, enthusiasm, and immense knowledge. His guidance helped me in all the time of research and writing of this thesis.

Many of my friends have of great emotional and physical help; they have kept me stay sane through these difficult months. Their support and care helped me overcome setbacks and stay focused on my graduate study. I greatly value their friendship and I deeply appreciate their belief.

No words can describe the thanks due to my friend **Eng. Ahmed Madani**, who always encourages and supports me.

DEDICATION

To the source of kindness, my aunts Afaf, Salma, Kawther, and Sara.

To my Brothers and sisters for they love and support.

To my colleagues Hala and Roa for they encourage.

To my lovely friends Amna, Gehad, Rabah and Salma for they support.

Hiba Doleib

Abstract

Quantitative elastography is a non-invasive imaging technique that studies the elastic properties of the tissue when force is applied, and gives quantitative information about it. In this research the present work was performed using static deformation on a breast mimic ultrasound phantom. Strain images are constructed from the measured radio frequency (RF) ultrasound signals. The mean strain is recovered from stiffer segmented lesion and from nearby normal tissue, and then compute strain ratio. The stiffness measurement was used to know whether there are already abnormalities in the breast tissue or not. The strain ratio value is a highly significant quantitative method for evaluating the stiffness degree of the breast mass. The result of calculation shows that the strain ratio was 0.4; which indicates that the lesion has less strain than background strain, moreover indicate there is a potential abnormality exist in the lesion area.

المستخلص

التحليل الكمي لمرونة الأنسجة هو عبارة عن طريقة تصوير غير اختراقية تقوم بدراسة خصائص المرونة للأنسجة عند تطبيق قوة ما، كما تقوم بإعطاء معلومات كمية عنها. في هذا البحث تم تنفيذ العمل الحالي باستخدام تشوه ثابت على فانتوم الموجات فوق الصوتية لمحاكاة الثدي.(Breast mimic ultrasound phantom) صور الالتواء Strain (images) تم استخلاصها من الموجات الراديوية (Radio frequency) المقاسة من إشارات الموجات فوق الصوتية .(Ultrasound signals) تم استرداد الالتواء من جزء من الكتلة الصلبة وبالقرب من الأنسجة الطبيعية ومن ثم تم حساب نسبة الالتواء Strain) .(ratioقياس الصلابة تم استخدامه لمعرفة هل هنالك تشوهات في أنسجة الثدي أم لا. قيمة نسبة الالتواء هي طريقة كمية ذات تحديد عالي لتقييم درجة الصلابة لكتلة الثدي. نتيجة الحسابات توضح أن نسبة الالتواء هي 0.4، والتي توضح ان الكتلة الصلبة لها التواء أقل من التواء الخلفية، وبالتالي توضح احتمالية وجود حالة غير طبيعية في مساحة الكتلة الصلبة.

Table of Contents

List of Figures

List of Abbreviations

Ultrasound	US
Conventional Ultrasound	CUS
Ultrasound Elastography	USE
Shear Wave Elastography	SWE
Region of Interest	ROIs
Confusion Assessment Method	CAM
Radio Frequencies	RF
Dynamic Programming	DP
Analytic Minimization	AM
Least Square Regression	LSR

Chapter One

Introduction

1.1 General View

Breast cancer is associated with high morbidity; ~1.38 million new cases and 458 000 deaths occur annually worldwide. Breast cancer is by far the most common cancer in females of both developed and developing countries, and remains a major public health problem.

Elastography is non-invasive imaging technique that studies elastic properties of soft tissue. It demonstrates abnormalities of both muscles and other tissue. In pathological conditions, tissue becomes stiffer than that of normal tissue. It is a newly developed dynamic technique that uses ultrasound (US) to provide an estimation of tissue stiffness by measuring the degree of distortion under the application of an external force. Hence, also known as 'palpation by imaging'.

Tissue elasticity measurement is useful for the diagnosis and differentiation of tumors. Sonoelastography is useful for the quantitative measurement of tissue stiffness. Conventional ultrasonography (CUS) is less accurate. Various ultrasound elastographic techniques like transient elastography, vibro-acoustography are used in clinical practice of which compression ultrasound elastography (USE) is most commonly used to evaluate difference in hardness between diseased tissue and normal tissue. [1]

Real time ultrasound elastography is newly developed technique which is semi quantitative, because it measures ratio between nodule and normal parenchyma, that use a dedicated software to provide an accurate measurement of tissue distortion. In examination it is important to maintain the level of pressure constant. US elastogram is displayed over the B-mode image in a color scale that ranges from red, for components with greatest elastic strain (*i.e.* softest components), to blue for those with no strain (*i.e.* hardest components), so it is a technique for contrast improvement.

Detection and characterization of breast tumors can be enhanced by using elastography which is able to differentiate between normal tissue and malignant tumors. [1] In addition it is a reliable, noninvasive, cost effective method helping to differentiate benign from malignant breast lesions, thus reducing the number of unnecessary interventional diagnostic procedures, would be valuable.
Although it is safe, simple and low cost image technique, there is limitations in penetration, especially on obese patients. Elastography conveys new information about internal tissue structure and behavior under load that is not otherwise obtainable.

It is also more sensitive than mammography because the sensitivity of the mammography increases with age, mammography is particularly sensitive for older women with fatty replaced breast tissue, but has a lower sensitivity in young women with dense breasts.

1.2 Problem Statement

Detection and characterization of breast tumors can be done using elastographic techniques. This study is mainly focused on the differentiation between normal tissue and malignant tumors of breast lesions. The main objective of this research is to introduce a new technique that can lead to reduce the need to further biopsies and surgical interferences when encountering the problem of classification of breast tumors. Detection of tumors is easier done by qualitative elastography, however, when classification is needed the quantitative elastography should be done to give more information about the tumor stiffness.

1.3 Objective

The objectives of this research are:

1.3.1 General Objective

The main aim of this research is to develop a technique as a second opinion for radiologist, to explore the breast tissue type in order to detect and classify breast lesions.

Utilization of quantitative elastography which is a key tool in classification of tumor types and grades.

1.3.2 Specific Objective

- To calculate tissue displacement.
- To calculate tissue strain.
- To develop new denoising method.
- To segment the object from the background.
- To calculate strain ratio for the lesion.

1.4 Thesis Layout

This dissertation consists of five chapters, chapter one is an introduction. Chapter two gives theoretical background and literature reviews. While the research methodology is describing in chapter three. The result obtained and discussion of the results are given in chapter four. Finally, chapter five is devoted for conclusion and recommendation.

Chapter Two

Theoretical Background and Reviews

This chapter aims to gives description of the theories leading to the detection of breast abnormality. Is divided into parts, part one is the theoretical background which aims to represent the importance of Elastography study and gives essential information on it is types, and the methods for estimating of the strain. Part two is reviews of available literature.

2.1 Theoretical Background

2.1.1 Elastography

B-mode ultrasound imaging, while an excellent all-round means of examining tissue, is poor at distinguishing stiff tissue from soft or compliant tissue. An important class of tissue, such as tumor tissue or cirrhotic tissue in the liver, grows out of the same tissue matrix material as the healthy tissue from which it is derived, and as a result, even though these types of tissue are stiffer or more fibrotic, they can be invisible under normal B-mode imaging. Elastography, a branch of tissue characterization, is the measurement and/or depiction of the elastic properties of tissues. It provides the missing image contrast needed to distinguish among the soft and stiff tissues. In pathological conditions, tissue becomes stiffer than that of normal tissue.

Elastography is a non-invasive imaging technique that helps in evaluation of elasticity of soft tissue in response to an applied force. Tissue elasticity measurement is useful for the diagnosis and differentiation of tumors. Sonoelastography is useful for the quantitative measurement of tissue stiffness. Conventional ultrasonography (CUS) is less accurate. Various ultrasound elastographic techniques like transient elastography, vibro-acoustography are used in clinical practice of which compression ultrasound elastography (USE) is most commonly used to evaluate difference in hardness between diseased tissue and normal tissue.

US waves travel with different velocities through tissues depending on their stiffness. Due to compression, tissue changes its mechanical properties and its reflection of US waves. Abnormal lesion deforms to lesser extent as compared to normal tissue as a result of tissue compression. In malignant tumors, tissues are stiffer than normal tissue. Elastography is used for the examination of organs like breast, thyroid and liver. [2-5]

2.1.2 Principle of Elastography

Principle underlying elastography is that when external or internal pressure is applied on tissue under investigation, it causes displacement within the tissue. [1,6] Malignant tissues are harder than normal surrounding tissues. [1] If the tissue is stiffer, displacement occurs to lesser extent and if tissue is softer, displacement is higher thus this displacement could be a measure of tissue hardness. Elastogram is an image that shows different shades of color corresponding to different degree of stiffness resulting from compression. [6] Images obtained by elastography are compared before and after compression. In same tissue, elasticity varies in different pathological conditions like inflammation and malignancy. [7] Figures 2.1.A and 2.1.B shows the principle of elastography.

Elasticity score is indicated by diverse colors. Range of these colors varies from red to blue. Red color indicates soft tissue, green color indicates tissue with intermediate stiffness and blue color represents hard tissue. [1,8]

2.1.3 Modalities of Elastography

Ultrasound Elastography.

Magnetic Resonance Elastography.

There are three forms of ultrasound elastography:

1. Shear waves ultrasound elastography. [8-9]

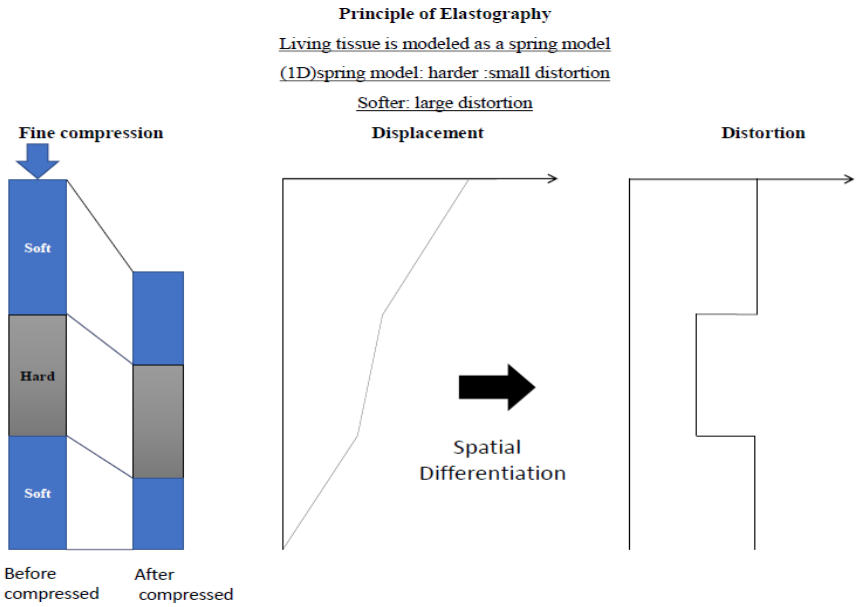

Fig 2.1.a Principle of Elastography. [15].

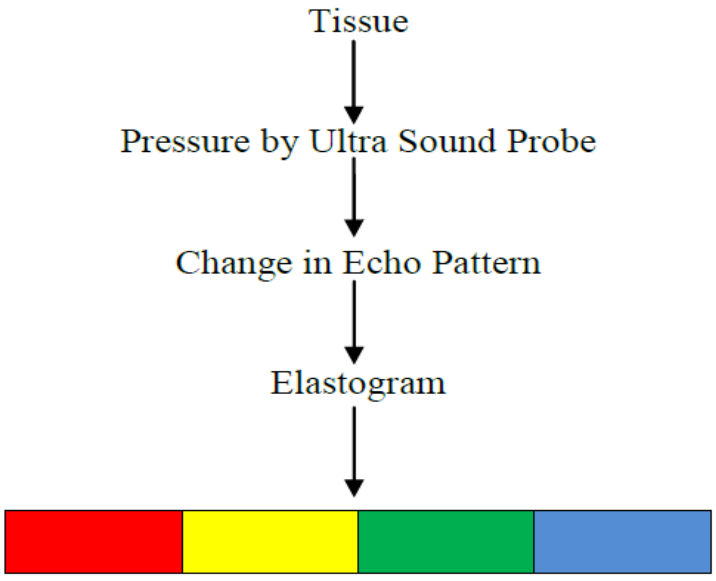

Fig 2.1.b Principle of Elastography. [15]

2. Quasi-static elastography.
3. Vibro-acoustography elastography.

2.1.3.1 Shear Wave Elastography (SWE)

In SWE, focused high intensity, short-duration acoustic pulse from ultrasound transducer are used to generate shear wave that absorb acoustic energy. [8,17] SWE requires fast attainment of ultrasound images ranging from 5000 to 20000 frames per seconds. [8] figure 2.2.A shows shear wave elastography.

2.1.3.2 Qusi-static Elastography

It is a very popular technique, in which external mechanical force or an endogenous force is applied to the tissue. [8,10-12] Number of images are taken before and after producing small deformation in the tissue. [13] Displacement and time delay that occur between region of interest (ROI) needs to be recorded at different compression. It is a qualitative technique.

Quality of result obtained is depended mainly on the experience and techniques of investigator. Appropriate compression strength and right angle of compression is necessary; otherwise there are chances of misinterpretation.

In order to obtain reproducible elastogram, compression has to be performed at least twice. [8-9,12,14] figure 2.2 B shows quasi-static ultrasound elastography.

2.1.3.3 Vibro-Acoustography Elastography

In this technique acoustic response of the tissue is used for imaging and material characterization. [12,14,16] For generating acoustic emission, two ultrasound beams of slightly different frequencies are used which are focused at same spatial point that vibrates the tissue because of ultrasound radiation force. For typical application of vibro-acoustography, two frequencies of order of 2-5MHz must be used and difference between the frequencies should be 10-70 kHz. With vibro-acoustography, it is possible to obtain the images that show some unique features that make it different from traditional ultrasound imaging.

vibro-acoustography provides quantitative estimation of viscoelastic parameter. Figure 2.2.C shows vibro-acoustography ultrasound elastography.

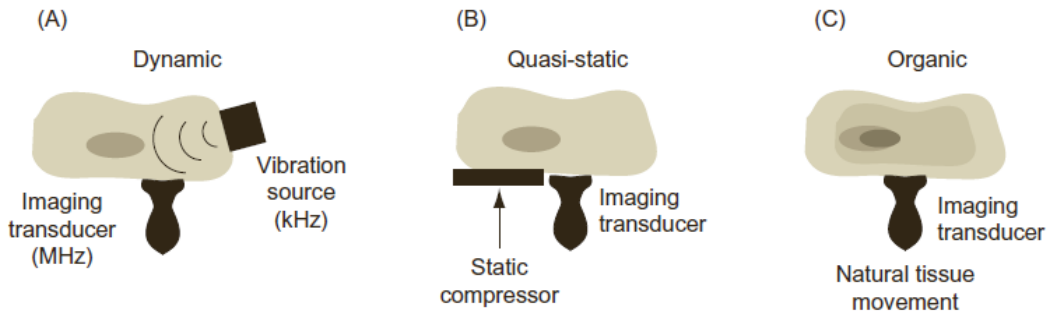

Fig 2.2 Main types of elastography. (A) Dynamic; (B) quasi-static; (C) organic. [15]

2.1.4 Methods for Measuring Strain

2.1.4.1 Spatial Correlation Method

Uses an ordinary two dimensional pattern-matching algorithms to search for the position that maximizes the cross correlation between regions of interest (ROIs) that are selected from two images (one obtained before and the other obtained after deformation).

2.1.4.2 Phase-Shift Tracking Method

Is based on an autocorrelation method that is well known as a principle of color Doppler ultrasonography determine longitudinal tissue motion because of phase domain processing. Because of errors related to aliasing, the phase-shift tracking method fails when used to measure large displacements. It poorly compensates for movement in the lateral direction.

2.1.4.3 Confusion Assessment Method (CAM)

Enables rapid and accurate detection of longitudinal displacement by using phase-domain processing without aliasing. A modification of CAM to

better demonstrate lateral and elevational tissue movements, inevitable during palpation-like freehand manipulation of the probe, is called extended CAM. The dynamic range of strain that is estimated by using the extended CAM is 0.05%–5.00% (optimal dynamic range, 0.50%–2.00%); this method can compensate for up to about 4 mm of lateral slip.

Traditionally, strain estimators aim to accurately derive tissue displacements between before and after compression and to compute strain from the displacements. However, the displacement can be as large as 1000 times the strain for typical compression levels used in US elasticity imaging. Error in displacement estimation leads to a large variance in strain, thereby resulting in poor signal-to-noise ratio for the estimated strain.

Bae and Kim have developed a novel strain estimator that can be used to directly estimate strain from the phase of temporal and spatial correlation instead of estimating small strain from large displacements. Signal-to-noise ratio and contrast-to-noise ratio of the elastogram measured by using the direct strain estimator are at least three times and six times larger, respectively, than values obtained by using conventional displacement-based strain estimators. This indicates that the direct strain estimator can substantially improve accuracy and lesion detectability in US elasticity imaging. In addition, the direct strain estimator is computationally efficient compared with conventional estimators, thus enabling the real-time implementation and clinical use of this new US imaging mode. [18]

2.2Literature Reviews

Reviews are the basis for discovery of which is the end of the first effort and at the same time the beginning of recent discoveries. So literature reviews were done to know the recent theories leading to the detection of breast cancer with good results, in order to do new method in order to achieve best result.

In this section, a few most important techniques for breast cancer detection are reviewed.

Jean Rossario Raj, Syed Mohammed Khalilur Rahman, Sneh Anand, proposed method using standard databases for breast cancer symptoms, mammography diagnosing features and breast cancer ultrasound elastography imaging screening standards, with ten dataset features as attributes. The adequate conditions of the features were considered for the classification as benign or malignant classes. The explanation criteria in elastography contain of the qualitative parameter elasticity score and the quantitative parameter strain ratio. Training of dataset was first done using 180 biopsy cases with 132 benign and 48 malignant results. 95% confidence interval for symptomatic was 1.625 to 4.955; mammographic was 1.506 to 5.494 and ultrasound elastography imaging was 2.213 to 6.087. The model created was further tested with 210 cases using three machine learning classifiers and results were compared with gold standard biopsy results. Performance characteristics were statistically analyzed. The three classifiers have yielded an accuracy of 95.7%, 84.3% and 91.4% respectively and the statistical models proved its efficiency in differentiating malignant from benign. [19] Xia Gong, Yi Wang, Weihua explored the values of ultrasound elastography as one of the more vital diagnostic tool in the diagnosing of breast lesions of US Breast lesions of Breast Imaging Reporting and Data System (BI-RADS) 4B by conventional ultrasound. Ultrasound elastography was used in a total of 151 US BI-RADS 4B patients who were diagnosed through the ultrasound and were surgically treated. The diagnosis of 188 benign and malignant lesions by ultrasound elastography was analyzed based on postoperative pathological examinations. As a results of this study, it can be concluded that the sensitivity, specificity and accuracy of the elastography in the diagnosis of breast lesion were 91.67% (66 of 72), 88.79% (103 of 116), and 89.89% (169 of 188) respectively. While using the ratio of 1.5 as a criterion to determine whether it is benign or malignant lesion, it resulted in slightly different result. The sensitivity, specificity and accuracy of ultrasound elastography were 90.28% (65 of 72), 87.93% (102 of 116) and 88.83% (167 of 188), respectively. [20] The main limitation of this study was that the false negative is relatively high, and it contradicts with the purpose of elastography in

reducing the false negative. Dana Stoian, Bogdan Timar, et al proposed method using a total of 174 patients, in which all of the 174 patients were diagnosed with dominant breast nodules. The results of the ultrasonography and real time elastography, both qualitative and quantitative, were compared with pathology findings from the biopsy specimens. The results were, pathology examinations determined 102 nodules were benign and 72 malignant. Qualitative elastography had a better diagnostic performance (82.4% sensitivity and 81.9% specificity) than ultrasonography plus Doppler evaluation (70.3% sensitivity and 73.5% specificity). Quantitative elastography, assessed using the fat-to-lesion ratio, was a good discriminant for malignancy (AUROC = 0.93, $p < 0.001$). Our results pointed to an optimal threshold for malignancy of > 4.88; by using this threshold, the diagnostic reliability of the fat-to-lesion ratio was better than both ultrasonography and the qualitative elastography (86.5% sensitivity and 90.4% specificity). [21] The problems that were faced in this study was caused by the fact that the value of FLR threshold is debatable. Different thresholds will give different diagnostic qualities. Ideally a recommended FLR Ratio, for each RTE device should be used in order to make a comparison between different studies. Young Jun Choi, Jeong Hyun Lee, Jung Hwan Baek proposed method that explore the diagnosing of strain elastography by examining a total of 141 lymph nodes, of which 98 were confirmed as benign and 43 were confirmed as malignant by histopathology. It classified the nodes according to visualization, brightness compared to the neighboring muscles, and the regularity of the outline. Using a strain ratio cut-off value of >1.5, strain elastography showed sensitivity, specificity, and accuracy values of 85%, 98%, and 92%, respectively. According to a recent meta-analysis of nine strain elastography studies that included 50-155 cervical or axillary lymph nodes [22], the pooled sensitivity and specificity values for detecting malignancies were 74% (95% confidence interval [CI], 66% to 81%) and 90% (95% CI, 82% to 94%) for elastographic scale and 88% (95% CI, 79% to 93%) and 81% (95% CI, 49% to 95%) using strain ratios, respectively. However, US elastography has many unresolved problems and limitations. The First problem is that the US

elastography can give unclear readings if there is a focal convex bulge on the skin overlying the ROI because, under those circumstances, it may be impossible to apply a linear transducer without producing focal stress concentrations within the tissue of interest, thereby resulting in spuriously stiff elastograms [22] Second, there are still issues regarding ROI selection in most studies on strain ratio or shear wave-based elastography. Third, the distance from the transducer, anisotropy, and stretch stress in overlying muscle all induce variations (Lee HY, unpublished observation). Fourth, cysts and calcified lesions lack elasticity. Fifth, highquality elastograms are often hard to obtain due to pulsations from nearby great vessels (Video clip 1). Finally, manufacturer-associated variations in the implementation of US elastography remain uncertain. Ashraf Ali Wahba, Nagat Mansour Mohammed Khalifa, et al Seddik1 developed a study success in recognizing breast tumor phantom by an average correct recognition ratio CRR of about 94.25% on a simulation environment. The strain ratio SR for benign and malignant models is also computed. The result of the simulated breast tumor model is compared with real data of 10 lesion cases (6 benign and 4 malignant). The coefficient of variation CV between the simulated SR and the SR using real data reaches to about 5% for benign lesions and 4.78% for malignant lesions. The results of CRR and CV in this work makes sure that the proposed breast cancer model using finite element modeling is a robust technique for breast tumor simulation where the behavior of breast cancer can be predicted. [23] The metric for this agreement is that if the coefficient of variation factor is around about 5% that indicates a good agreement. Alessandro Ramalli, Luca Bassi, et al, proposed method using freehand elastography method, based on a Fourier domain displacement estimator, it has been recently re-researched and it proved to be capable of producing off-line robust estimates of phantoms elasticity. In order to permit in-vivo examinations of breast lesions, a real-time version of the proposed method has been places in the research scanner ULA-OP, designed at the University of Florence. In a preliminary test on patients the method detected 36 lesions (11 softer, 14 harder and 11 having the same elasticity than the surrounding tissue).

The same lesions were classified as malignant (5) and benign (31) by an experienced sonographer through B-mode analysis. [24]Xue-Jing Liu, Ying Zhu, et al, presented study aimed to analysing and comparing the diagnostic performance of B-mode ultrasound (US), elastography score (ES), and strain ratio (SR) for the differentiation of breast lesions. This retrospective study enrolled 431 lesions from 417 in-hospital patients. All patients were examined with both conventional ultrasound and elastography. Two experienced radiologists reviewed the ultrasound and elasticity images. The histopathologic result obtained from ultrasound-guided core biopsy or operation excisions were used as the standard. Pathologic examination revealed 276 malignant lesions (64%) and 155 benign lesions (36%). A cut-off point of 4.15 (area under the curve, 0.891) allowed significant differentiation of malignant and benign lesions. ROC (receiver-operating characteristic) curves showed a higher value for combination of B-mode ultrasound and elastography for the diagnosis of breast lesions. [25] The limitations of this study were that conventional ultrasound combined elastography showed high sensitivity, specificity, and accuracy for lesions with diameter (10mm<lesion diameter ≤20mm). Also when the tumor volume is small, the difference in hardness between the benign lesions and normal breast tissue is less, due to which the elastic strain is also small; hence, the elasticity image is green. Furthermore, there was misdiagnosed cases on elastogram, we found that calcification, fibrosis, and necrosis within the lesion were important factors that could alter the texture of lesions and cause misdiagnosis. When size of the breast lesions is large, these factors may be present within the area resulting in uneven hardness in the lesions. In such cases, the elasticity images are manifested in blue and green, but an elasticity score of 2-5 points may lead to false negative results. Deniz Cebi Olgun, Bora Korkmazer, et al**,** presented study aimed to determine the correlations between the elasticity values of solid breast masses and histopathological findings to define cutoff elasticity values differentiating malignant from benign lesions. A total of 115 solid breast lesions of 109 consecutive patients were evaluated prospectively using shear wave elastography (SWE). Two orthogonal

elastographic images of each lesion were obtained. Minimum, mean, and maximum elasticity values were calculated in regions of interest placed over the stiffest areas on the two images; it is also calculated mass/fat elasticity ratios. Correlation of elastographic measurements with histopathological results were studied. Eighty-three benign and thirty-two malignant lesions were histopathologically diagnosed. The minimum, mean, and maximum elasticity values, and the mass/fat elasticity ratios of malignant lesions, were significantly higher than those of benign lesions. The cutoff value was 45.7 kPa for mean elasticity (sensitivity, 96%; specificity, 95%), 54.3 kPa for maximum elasticity (sensitivity, 95%; specificity, 94%), 37.1 kPa for minimum elasticity (sensitivity, 96%; specificity, 95%), and 4.6 for the mass/fat elasticity ratio (sensitivity, 97%; specificity, 95%). [26] This study had some limitations. First, not all histological types of malignant and benign lesions were represented. Multicenter studies are needed to overcome this limitation. Second the interobserver was not assessed variability but the method has been shown previously to be highly reproducible. Brett Coelho, developed method using clinical ultrasound elastography based on strain imaging that determines tissue stiffness but not the true Young's modulus distribution. Furthermore, the stress uniformity assumption associated with strain imaging result of poor sensitivity and specificity of this clinical tool. To enhance this technique, the strain image can be processed for tissue elastic modulus reconstruction. The proposed technique is to calculate stress value using Finite Element Method (FEM) and reconstructed the Young's modulus distribution using Hooke's law until the desired values are achieved. Since tissue geometry is difficult to obtain using strain imaging, the proposed methods is unconstructed and does not require tissue geometry. The strain images of the prostate phantom were processed using this computationally intensive method in order to validate the technique. The results were used to assess the effectiveness of it as a clinical tool for cancer diagnosis. [27] Limitations of this study was that the manual selection of tissue regions and tumor sites incorporate inter observer variability as a potential source of error, FEM boundary conditions could potential be improved and

implementing a finer FEM mesh would lead to greater resolution, Ultimately the method should be improved to better locate tumors and calculate the Young's modulus ratios in order to diagnose prostate cancer more effectively. Finally, a faster program should replace abacus to allow post processing to be performed in real time, considering it required several minutes to perform the iterative technique. E. Fiorini, V. Cipriano, et al, proposed method calculating liver stiffness with RTE in patients with chronic viral hepatitis and to assess the possible correlation between RTE data and the degree of fibrosis based on liver biopsy findings (Ishak score). 26 patients (18M, 8F, mean age 41±13 [standard deviation], range 22-62) with chronic viral hepatitis were prospectively evaluated with ultrasonography (US) that included RTE. All patients then underwent US-guided percutaneous liver biopsy (right lobe) for evaluation of fibrosis. Examinations were done with a iU22 scanner (Philips, Bothell, WA, USA); a convex transducer (C5-1) was used for the US examination, and a linear transducer (L12-5) for RTE. In the RTE images, relative tissue stiffness is conveyed according to a color scale with soft areas represented in green/red and hard areas in blue. Patients were examined in the supine position in suspended normal respiration; three loops of 20 RTE frames were recorded for each case. For each patient, we calculated the mean strain ratio (MSR) for the 3 loops. The Spearman correlation coefficient was used to assess correlation between the ASR and fibrosis stage (F) reflected by the Ishak score. The Spearman coefficient showed significant correlation between the MSR and F (Rho = 0.470, p = 0.015). RTE seems to be a valuable tool for noninvasive evaluation of fibrosis in patients with chronic viral hepatitis although these findings need to be confirmed in larger case series. [28] Hassan Rivaz, Emad M. Boctor, et al, produced two real-time elastography techniques that depend on analytic minimization (AM) of regularized cost functions. The former method (1D AM) gives axial strain and integer lateral displacement, while the later method (2D AM) gives both axial and lateral strains. The cost functions integrate similarity of RF data intensity and displacement continuity, generating both AM methods firm to small decorrelations occur throughout the image**.** Also it was used

Kalman filter to calculate the strain field from the displacement field given by the AM methods. Simulation and phantom experiments showing that the both methods give strain images with high SNR, CNR. [29] Angelica Chiorean, Maria Magdalena, Duma et al, developed method based on pre – and post compression data. According to the equipment type, various colors (256 hues) or gray shades are super imposed on 2D image. Stiff areas are coded in blue or dark gray tins, while softer, elastic tissue appear in red, green or bright shades of gray. The examination protocol was in accordance with Hitachi guidelines for elastography and final assessment was based on principles of Tsukuba elasticity score. [30] The limitation of this study was that the reported sensitivity and specificity of sonoelastography ranged between 77.9_96%, 87_91.5% respectively. The higher values were obtained with the assessment of smaller lesions, under 2 cm in diameter. It is also influenced by breast type; a higher sensitivity being observed for adipose breasts. Furthermore, has a limited application in very dense, fibrous parenchyma, in case of hematomas or breast implants. Hassan Rivaz, Emad Boctor, proposed study a 2-D strain imaging technique based on minimizing a cost function using dynamic programming (DP). The cost function integrates similarity of echo amplitudes and displacement continuity. Because tissue deformations are smooth, the integration of the smoothness into the cost function results in minimize decorrelation noise. The output of the method gives high-quality strain images of freehand palpation elastography with up to 10% compression, which shows that the method is more firm to signal decorrelation in comparison to the standard correlation techniques. The operation of the method is less than 1s and it is also appropriate for real time elastography. [31] Claire Pellot-Barakat, Mallika Sridhar, et al, explored method summarizes several approaches to breast elasticity imaging to explain some of the observed variability in breast imaging results. Preliminary clinical results from 13 patients with small and nonpalpable breast lesions obtained with a low noise elasticity imaging algorithm developed in the group and are then reported. All the benign lesions exhibited normal elasticity ranges. About half of the malignant lesions were undetected with

elasticity imaging most likely because of their small size (<7mm) or softening from the addition of fatty-replaced tissue. Other malignant lesions were clearly identified as areas with extreme elasticity values compared to their surroundings. We observed that some malignant lesions did not exhibit any desmoplasic stiffening while others showed an uncommon softening. It is clear that by broadening the study population to include small and nonpalpable lesions, we see much variability in elasticity image findings. [32] All the benign lesions in this study exhibited normal elasticity ranges, as expected for many benign masses. Among the 7 malignant lesions, 2 nonpalpable lesions were clearly detected as areas with extreme elasticity values compared to the surrounding tissue while 2 malignant lesions could not be identified with elasticity imaging. The 3 other malignant lesions did not exhibit striking elasticity patterns but had either high or low displacements, and this could be considered the limitation of this study.

Chapter Three

Material and Methodology

3.1 Methodology

The proposed method was developed using Matlab 2016 platform. The algorithm started with loading raw RF data to Matlab from breast elastography phantom, using B-mode ultrasound, manufactured by Siemens with central frequency of 6.67 MHz. Then axial and lateral displacements were obtained from the raw RF data using the 2D analytical minimization. Moreover, the least square regression approach was utilized to obtain the two strain images namely axial and lateral strain images as shown in figure.3.1. Then, the resultant images were filtered using the Kalman filter which enhanced the appearance of the strain images with minimal blurring. After that the region of interest (ROI) was segmented using the region growing segmentation to calculate the strain ratio, diameter and area. Strain ratio was calculated to determine tissue stiffness.

3.1.1 Elastography

Let $I_1$and I_2 be two images obtained from the tissue before and after the deformation. Letting I_1 and I_2 be of size M×N (Figure3.2). The goal is to find two matrices A and L where the $(i,j)^{th}$component of A ($\alpha_{i,j}$) and L ($l_{i,j}$) are the axial and lateral motion of the pixel (i,j) of I_1 .The axial and lateral strains are easily calculated by spatially differentiating A in the axial direction (resulting in A_α) and L in the lateral direction (resulting in L_l).

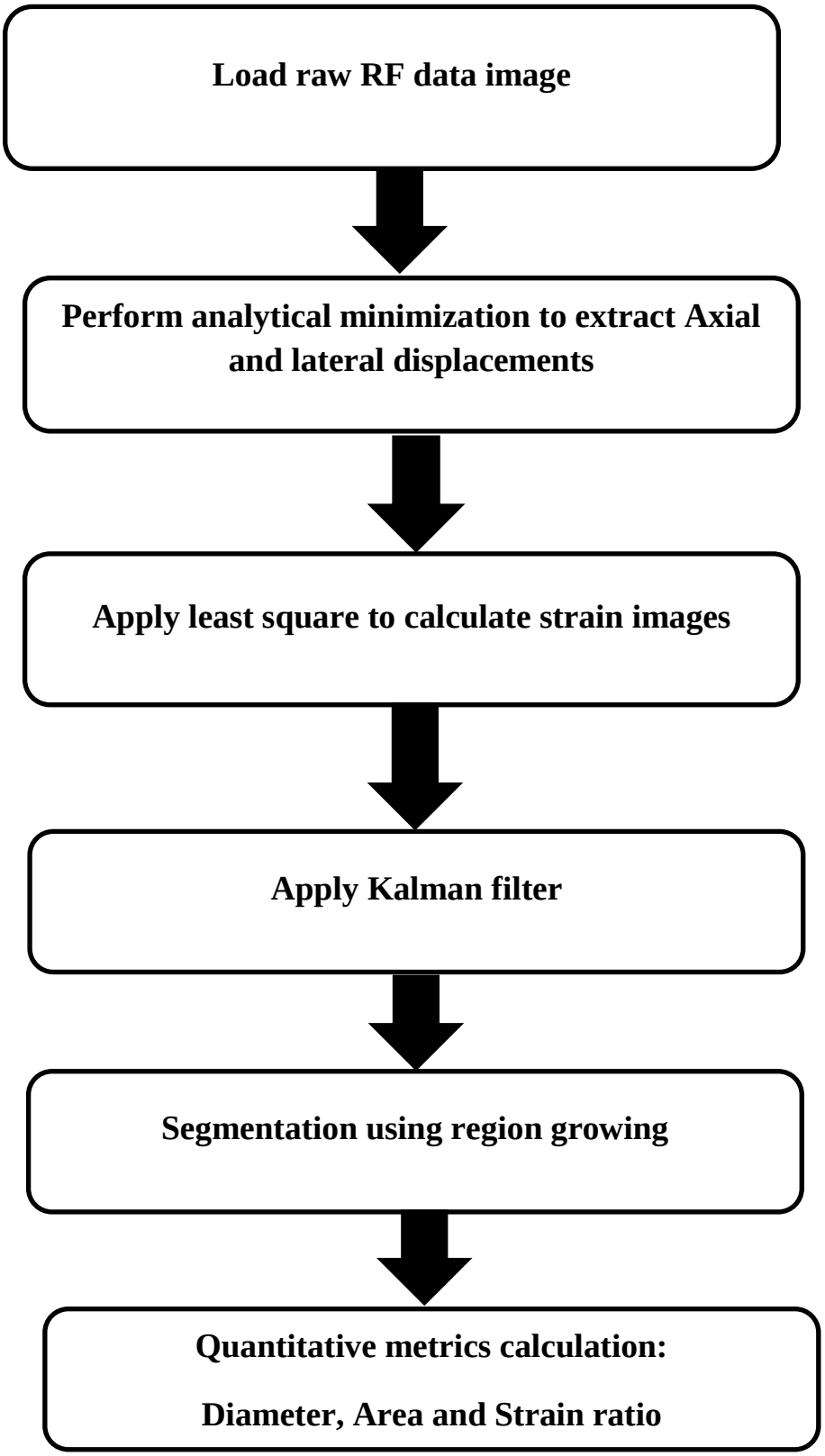

Fig. 3.1 Block diagram of the proposed method

3.1.1.1Dynamic Programming (DP)

Towards present the general formation of DP , we reflect a single column j (an RF-line) in I_1 (the image before deformation) in Figure 3.1 Let m and n be the length of the RF-lines and the number of RF-lines in the images (Figure3.1.1). Let a_i and l_i refer to the axial and lateral displacements of the i^{th} sample of the RF-line in column j. In DP elastography [31], a regularized cost function is generated by adding the prior of displacement continuity (the regularization term) to an amplitude similarity term. The displacement continuity term for column j is

$$R_j(a_i, l_i, a_{i-1}, l_{i-1}) = \alpha_a(a_i - a_{i-1})^2 + \alpha_l(l_i - l_{i-1})^2 \quad (3.1)$$

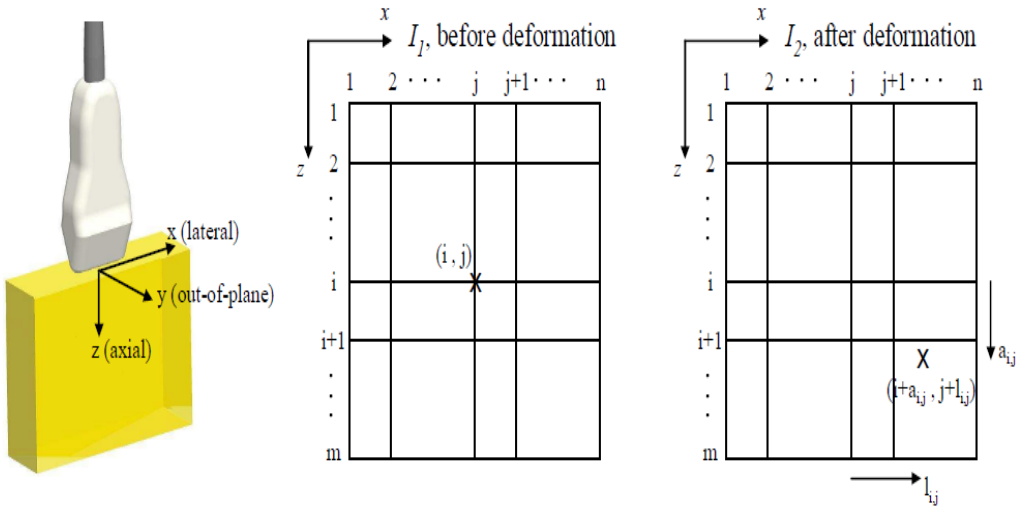

Fig.3.2 Axial, lateral and out-of-plane directions. The coordinate system is attached to the ultrasound probe. The sample (i, j) marked by x moved by $(\alpha_{i,j}, l_{i,j})$. where $\alpha_{i,j}$ and $l_{i,j}$ are respectively axial and lateral displacements and initially are integer in dynamic programing. [29]

which forces the displacements of the sample i (i.e. a_i and l_i) be similar to the displacements of the previous sample i-1 (i.e. a_{i-1} and l_{i-1}). α_a and α_l are axial and lateral regularization weights respectively. We write $R_j(a_i, l_i, a_{i-1}, l_{i-1})$ to

indicate the dependency of a_i and l_i on j. The regularized cost function for column j is then generated as following

$$C_j(a_i, l_i, i) = [I_1(i,j) - I_2(i + a_i, j + l_i)]^2 + \min_{da,dl} \left\{ \frac{C_j(d_a, d_l, i-1) + C_{j-1}(d_a, d_l, i)}{2} + R_j(a_i, l_i, d_a, d_l) \right\} \quad (3.2)$$

where d_a and d_l are temporary displacements in the axial and lateral directions that are varied to minimize the term in the bracket. After calculating C_j for i = 2,…,m , C_j is minimized at i = m giving α_m and l_m. The α_i and l_i values that have minimized the cost function at i = m are then traced back to i = 1, giving integer α_i and l_i for all samples of line j^{th} . The process is performed for the next line j + 1 until the displacement of the whole image is calculated.

3.1.1.2 Analytic Minimization (AN)

Tissue deformations in ultrasound elastography are usually very small and therefore a subsample displacement estimation is required. We now develop a method that analytically minimizes a regularized cost function and gives the refined displacement field following the work presented in [33]. We first consider a specialization of Equation 3.2 in which we only consider refining axial displacements to subsample level.

Having the integer displacements a_i and l_i from DP, it is desired to find Δa_i values such that $a_i + \Delta a_i$ gives the value of the displacement at the sample i for i = 1,…,m (l_i ,a_i and Δa_i correspond to line j. Hereafter, wherever the displacements correspond to thej^{th} line, j is omitted to prevent notation clutter). Such Δa_i values will minimize the following regularized cost function

$$C_j(\Delta a_1, \dots, \Delta a_m) = \sum_{i=1}^{m} \{ [I_1(i,j) - I_2(i, a_i + \Delta a_i, j + l_i)]^2 + \alpha_a (a_i + \Delta a_i - a_{i-1} - \Delta a_{i-1})^2 + \alpha_l (a_i + \Delta a_i - a_{i,j-1} - \Delta a_{i,j-1})^2 \} \quad (3.3)$$

where $\alpha_a > 0$ and $\alpha_l > 0$ are tunable axial and lateral regularization weights and subscript j-1 refers to the previous RF-line (adjacent RF-line in the lateral direction). Substituting I_2 ($i+d_i+\Delta d_i$) with its first order Taylor expansion approximation around d_i we have

$$C_j\,(\Delta a_1,\dots,\Delta a_m)=\sum_{i=1}^{m}\{[I_1\,(i,j)-I_2\,(i,a_i\,,j+l_i)-I'_2(i+a_i\,,j+l_i)\Delta a_i]^2+$$
$$\alpha_a\,(a_i+\Delta a_i-a_{i-1}-\Delta a_{i-1})^2+\alpha_l\,(a_i+\Delta a_i-a_{i,j-1}-\Delta a_{i,j-1})^2\}\qquad(3.4)$$

where I'_2 is the derivative of the I_2 in the axial direction. The optimal Δa_ivalues occur when the partial derivative of C_j with respect to Δa_i is zero. Setting $\frac{\partial C_j}{\partial \Delta a_i}=0$ for i =1,..,m we have

$$\left(I'^{2}_{2}+\alpha_a\,\Delta+\alpha_l\hat{I}\right)\Delta a_j=I'_2 e-\left(\alpha_a D+\alpha_l\hat{I}\right)a_j+\alpha_l a_{j-1}\quad(3.5)$$

$$D=\begin{bmatrix}1 & -1 & 0 & 0 & \cdots & 0\\ -1 & 2 & -1 & 0 & \cdots & 0\\ 0 & -1 & 2 & -1 & \cdots & 0\\ \vdots & & & & \ddots & \\ 0 & 0 & \cdots & 0 & -1 & 1\end{bmatrix}\qquad(3.6)$$

where I'_2 $\mathrm{diag}(I'_2(1+d_1,j+l_i)-I'_2(m+d_m,j\,l_i))$,$\Delta a_j$ $\left[\Delta a_{1,j}\ \dots \Delta a\ \ m,j\right]^T$, e= $[e_1\dots e_m]^T$, $e_i=I_1(i,j)-I_2(i+d_i,j+l_i)$,$a_j=\left[a_{1,j}\dots a_{m,j}\right]^T$, $\hat{I}$ is the identity matrix and a_{j-1} is the total displacement of the previous line (i.e. when the displacement of the $j-1^{th}$ line was being calculated, a_{j-1} was updated with $(a_{j-1}+\Delta a_{j-1})$, I'_2, D and $\hat{I}$ are matrices of size $m\times m$and Δa, e and a are vectors of size m..

Comparing 1D AM (as formulated in Equation 3.5) and 2D DP, they both optimize the same cost function. Therefore, they give the same displacement fields (up to the refinement level of the DP). In the next two subsections, we will further improve 1D AM.

1) Biasing the Regularization: The regularization term $\alpha_a(a_i+\Delta a_i-a_{i-1}-\Delta a_{i-1})^2$ penalizes the difference between $a_i+\Delta a_i$ and $a_{i-1}+\Delta a_{i-1}$, and therefore can result in underestimation of the displacement field. Such underestimation can be prevented by biasing the regularization by ϵ to $\alpha_a(a_i+\Delta a_i-a_{i-1}-\Delta a_{i-1}-\epsilon)^2$, where $\epsilon=(a_m-a_1)/(m-1)$is the average displacement difference (i.e. average strain) between samples i and i-1. An accurate enough estimate of d_m-d_1 is known from the previous line. With the bias term, the

R.H.S. of Equation 3.5 becomes $I_2'e - (\alpha_a D + \alpha_l \hat{I})a_j + \alpha_j(a_{j-1} + \Delta a_{j-1}) + b$where the bias term is $b = \alpha_a[-\epsilon\ 0 \ldots 0\ \epsilon]^T$(only the first and the last terms are nonzero) and all other terms are as before. In the other words, except for the first and the last equations in this system, all other m-2 equations are same as Equation 3.5.

Equation 3.5 can be solved for Δa_j in 4m operations since the coefficient matrix $I_2' + \alpha_a D + \alpha_l \hat{I}$is tridiagonal. Utilizing its symmetry, the number of operations can be reduced to 2m. The number of operations required for solving a system with a full coefficient matrix is more than m3=3, significantly more than 2m.

2) Making Elastography Resistant to Outliers: Even with pure axial compression, some regions of the image may move out of the imaging plane and decrease the decorrelation. In such parts the weight of the data term in the cost function should be reduced. The data from these parts can be regarded as outliers and therefore a robust estimation technique can limit their effect. Before deriving a robust estimator for Δa, we rewrite Equation 3.4 as

$$C(\Delta a) = \sum_{i=1}^{m} \rho(r_i) + R(\Delta a) \qquad (3.7)$$

Where r_i = $I_1(i)$-$I_2(i + a_i) - I_2'(i + a_i)\Delta a$ is the residual, $\rho(r_i)$ = ${r_i}^2$ and R is the regularization term. The M-estimate of Δa is $\Delta\hat{a} = \arg\min_{\Delta a}\{\sum_{i=1}^{m} \rho(r_i) + R(\Delta a)\}$ where $\rho(r_i)$ is a robust loss function [34]. The minimization is solved by setting $\frac{\partial C}{\partial \Delta a_i} = 0$

$$\rho'(r_i)\frac{\partial r}{\partial \Delta a_i} + \frac{\partial R(\Delta a)}{\partial \Delta a_i} = 0 \qquad (3.8)$$

A common next step [35] is to introduce a weight function w, where $w(r_i)$. $r_i = \rho'(r_i)$. This leads to a process known as "iteratively reweighted least squares" (IRLS) [36], which alternates steps of calculating weights w (r_i) for r_i = 1…m using the current estimate of Δa and solving Equation 3.8 to estimate a

new Δa with the weights fixed. Among many proposed shapes for w(.), we compared the performance of Huber [34-35]

$$w(r_i) = \begin{cases} 1 & |r_i| < T \\ \frac{T}{|r_i|} & |r_i| > T \end{cases} \qquad (3.9)$$

And Cauchy [36]

$$w(r_i) = \frac{1}{1+(r_i/T)^2} \qquad (3.10)$$

functions and discovered that the stricter Cauchy function (which decreases with inverse of the square of the residual) is more suitable in our application. To better discriminate outliers, we calculate the residuals r_i at linear interpolation of the integer sample displacements provided by DP. With the addition of the weight function, Equation 3.8 becomes

$$(wI_2' + \alpha_a D + \alpha_l \hat{I})\Delta a_j = wI_2' e - (\alpha_a D + \alpha_l \hat{I})a_j + \alpha_j a_j + b \qquad (3.11)$$

Where w=diag $(w(r_1)\ldots w(r_m))$. This equation will converge to a unique local minimum after few iterations [36]. The convergence speed however depends on the choice of T, which in this work is defined manually. Since the Taylor approximation gives a local quadratic approximation of the original non-quadratic cost function, the effect of higher orders terms increase if $\Delta a_j$is large. Assuming that DP gives the correct displacements, $\|\Delta a_j\|_\infty \leq \epsilon$ where $\|.\|_\infty$ is the infinity norm and $\epsilon \leq 0.5$. In practice, however, $\epsilon \ll 0.5$ because the linear interpolation of the DP displacements (which is very close to the correct displacement) is used to calculate the residuals r_i. Therefore, a small value can be assigned to T in 1D AM provided that DP results are trusted.

The coefficient matrix $Q = wI_2'^2 + \alpha_a D + \alpha_l \hat{I}$ Equation 3.11 is the Hessian of the cost function C whose minimum is sought. This matrix is strictly diagonally dominant (i.e. $|q_{ii}| > \sum j \neq i |q_{ij}|$for all i where q_{ij} is the i ,j^{th} element of Q), symmetric and all diagonal entries are positive. Therefore, it is positive definite,

which means that setting the gradient of C to zero results in the global minimum of C (not in a saddle point, a local maximum or a local minimum). All of the 1D AM results presented in this work are obtained with one iteration of the above equation.

1D AM takes the integer axial and lateral displacement fields from DP and gives refined axial displacement. It inherits the robustness of DP and adds more robustness when calculating the fine axial displacements via IRLS. However, there are redundant calculations in this method which are eliminated in 2D AM as described next.

In 2D AM, we modify Equation 3.2 to calculate subsample axial and lateral displacement fields simultaneously. The outline of our proposed algorithm is as follows

1. Calculate the integer axial and lateral displacements of one or more seed RF-lines (preferably in the middle of the image) using DP (Equation 3.2). Calculate the linear interpolation of the integer displacements as an initial subsample estimate.
2. Calculate subsample axial and lateral displacements of the seed RF-line using 2D AM, as explained below. Add the subsample axial and lateral displacements to the initial estimate to get the displacement of the seed line.
3. Propagate the solution to the right and left of the seed RF-line using the 2D AM method, taking the displacement of the previous line as the initial displacement estimate.

Benefits of 2D AM are two-fold. First it computes subsample displacements in both axial and lateral directions. Lateral strain contains important information from tissue structure that is not available from axial strain [37-39]. Second, it is only required to calculate the displacement of a single line using DP (the seed), eliminating the need to have the integer displacement map for the entire image. This is significant as in the 1D AM method, the initial step to calculate the 2D integer displacements using DP takes about 10 times more than the 1D AM.

Assume that initial displacement estimates in the axial direction, a_i, and in the lateral direction, l_i, are known for all i = 1 … m samples of an RF-line. Note that a_i and l_i are not integer; for the seed line they are the linear interpolation of the integer DP displacements and for the rest of the lines are the displacement of the previous line. It is desired to find $\Delta a_i$and Δl_i values such that the duple $(a_i + \Delta a_i, l_i + \Delta l_i)$ gives the axial and lateral displacements at the sample i. Such $\Delta d_i, \Delta a_i$values will minimize the following regularized cost function

$$C_j(\Delta a_1, \dots, \Delta a_m, \Delta l_1, \dots, \Delta l_m)$$
$$= \sum_{i=1}^{m} \{[I_1(i,j) - I_2(i + a_i + \Delta a_i, j + l_i + \Delta l_i]^2$$
$$+ \alpha(a + a_i + \Delta a_i - a_{i-1} - \Delta a_{i-1})^2 + \beta_a(l_i + \Delta l_i - l_{i-1} - \Delta l_{i-1})^2$$
$$+ \beta'_l\left(l_i + \Delta l_i - l_{i,j-1}\right)^2)\} \qquad (3.12)$$

where I(i,j) is the i^{th} sample on the j^{th} RF-line. Since we perform the calculations for one RF-line at a time, we dropped the index j to simplify the notations:a_i, Δa_i, $l_i$and $\Delta l_i$are $a_{i,j}$, $l_{i,j}$, $\Delta a_{i,j}$ and $\Delta l_{i,j}$. $l_{i,j-1}$ is the lateral displacement of the previous RF-line (note that $l_{i,j-1}$ is the total lateral displacement of the previous line, i.e. when the displacement of the $j-1^{th}$line was being calculated, $l_{i,j-1}$ was updated with $l_{i,j-1} + \Delta l_{i,j-1}$). Since in the first iteration a_i and l_i (the initial displacement estimates) are in fact the displacements of the previous RF-line, for the first iteration we have $l_{i,j-1} = l_i$. This simplifies the last term in the R.H.S. to $\beta'_l \Delta l^2_i$ .The regularization terms are α, $\beta_a$and β'_l. α determines how close the axial displacement of each sample should be to its neighbor on the top and β_a and β'_ldetermine how close lateral displacement of each sample should be to its neighbors on the top and left (or right if propagating to the left). If the displacement of the previous line is not accurate, it will affect the displacement of the next line through the last term in the R.H.S. of Equation 7. Although its effect will decrease exponentially with j, it will propagate`e for few RF lines. Therefore, we set

$$\beta'_l = \frac{\beta_l}{1+|r_{i,j-1}|} \qquad (3.13)$$

to prevent such propagation where $r_{i,j-1}$ is the residual associated with the displacement of the i^{th} sample of the previous line. A large residual indicates that the displacement is not accurate and therefore its influence on the next line should be small, which is realized via the small weight β'_l . This is, in principle, similar to guiding the displacement estimation based on a data quality indicator [40]. The effect of the tunable parameters α, $\beta_a$and β'_l is studied in the Results section. Writing the 2D Taylor expansion of the data term in Equation 7 around $(i + a_i, j + l_i)$:

$$I_2(i + a_i + \Delta a_i, j + l_i + \Delta l_i) \approx I_2(i + a_i, j + l_i) + \Delta a_i I'_{2,a} + \Delta l_i I'_{2,l} \qquad (3.14)$$

where $I'_{2,a}$ and $I'_{2,l}$ are the derivatives of the I_2 at point $(i + a_i, j + l_i)$ in the axial and lateral directions respectively. Note that since the point $(i + a_i, j + l_i)$ is not on the grid a_i and l_i are not integer), interpolation is required to calculate $I'_{2,a}$ and $I'_{2,l}$. We propose a method in Section II-C1 that eliminates the need for interpolation. The optimal (Δa_i, Δl_i) values occur when the partial derivatives of C_j with respect to both $\Delta a_i$and $\Delta l_i$are zero. Setting $\frac{\partial C_j}{\partial \Delta a_i} = 0$ and $\frac{\partial C_j}{\partial \Delta l_i} = 0$ for i = 1…m and stacking the 2m unknowns in $\Delta d = [\Delta a_1 \Delta l_1 \Delta a_2 \Delta l_2 \dots \Delta a_m \Delta l_m]^T$ and the 2m initial estimates in $d = [a_1 l_1 a_2 l_2 \dots a_m l_m]^T$ we have

$$(I'^2{}_2 + \mathcal{D}_1 + \mathcal{D}_2)\Delta d = I'_2 e - \mathcal{D}_1 d \qquad (3.15)$$

$$\mathcal{D}_1 = \begin{bmatrix} \alpha & 0 & -\alpha & 0 & 0 & 0 & \cdots & 0 \\ 0 & \beta_a & 0 & -\beta_a & 0 & 0 & \cdots & 0 \\ -\alpha & 0 & 2\alpha & 0 & -\alpha & 0 & \cdots & 0 \\ 0 & -\beta_a & 0 & 2\beta_a & 0 & -\beta_a & \cdots & 0 \\ 0 & 0 & -\alpha & 0 & 2\alpha & 0 & \cdots & 0 \\ \vdots & & & & & & \ddots & \\ 0 & 0 & 0 & \cdots & -\alpha & 0 & \alpha & 0 \\ 0 & 0 & 0 & \cdots & 0 & -\beta_a & 0 & \beta_a \end{bmatrix}$$

where $\mathcal{D}_2$ = diag(0, β'_1,0, β'_1,…,0, β'_1) is a diagonal matrix of size $2m \times 2m$, $I'^2{}_2$= diag($\mathcal{J}'^2(1) \dots \mathcal{J}'^2(m)$) is a symmetric tridiagonal matrix of size $2m \times 2m$ with

$$\mathcal{J}'(i) = \begin{bmatrix} {I_{2,a}}'^2 & {I_{2,a}}' {I_{2,l}}' \\ {I_{2,a}}' {I_{2,l}}' & {I_{2,l}}' \end{bmatrix} \qquad (3.16)$$

blocks on its diagonal entries where ${I_{2,a}}'$ and ${I_{2,l}}'$ are the derivatives of the I_2 at point $(i + a_{i,j} + l_i)$ in the axial and lateral directions,

$$I_2' = \mathrm{diag}({I_{2,a}}'(1), {I_{2,l}}'(1), {I_{2,a}}'(2), {I_{2,l}}'(2) \dots {I_{2,a}}'(m), {I_{2,l}}'(m)) \qquad (3.17)$$

Where ${I_{2,a}}'(i)$ and ${I_{2,l}}(i)'$ are calculated at point $(i + a_{i,j} + l_i)$, and $e = [e_1 e_1 e_2 e_2 \dots e_m]^T, e_i = I_1(i,j) - I_2(i + a_{i,j} + l_i)$.

We make four modifications to Equation 3.15: First we take into account the attenuation of the ultrasound signal with depth. As the signal gets weaker with depth, the first term in the R.H.S. of Equation 3.15 ($I_2'e$) gets smaller. This results in increasing the share of the regularization term in the costC_j and therefore over-smoothing the bottom of the image.

The attenuation of the ultrasound signal [41] reflected from the depth d is $\varsigma(d) = e^{-2\log(10)a_t f_0 d/20}$where a_t is the frequency dependent attenuation coefficient of tissue and is equal to 0.63 dB/cm/MHz for fat [41], f_0 is the center frequency of the wave (in MHz) and d is in cm. Having the exponential attenuation equation, the attenuation level at sample i will be

$$\zeta_i = x^{-i}, x = e^{\frac{1540\times10^2 a_t f_0 \log(10)}{20 f_s \times 10^6}}, \quad i=1\dots m \qquad (3.18)$$

Where the 1540×10^2 is the speed of sound in tissue (in cm/sec) and f_s is the sampling rate of the ultrasound system (in MHz). This is assuming that the TGC (time gain control) is turned off. Otherwise, the TGC values should be taken into account in this equation. Let the $2m \times 2m$ diagonal matrix Z be $Z = \mathrm{diag}(\zeta_1 \zeta_1 \zeta_2 \zeta_2 \dots \zeta_m \zeta_m)$. To compensate for the attenuation, we multiply the D_1 and D_2 matrices in Equation 3.15 by Z, and therefore reduce the regularization weight with depth. The regularization weight can vary substantially with no performance degradation. Therefore, approximate values of the speed of sound and attenuation coefficient will suffice. Second, we add a bias term in the regularization similar to the 1D case. Here we only bias the axial displacement

since the difference between the lateral displacements of the points on a RF-line is very small, usually less than 4 RF-lines. Third, we exploit the fact that, because the tissue is in contact with the ultrasound probe, the axial displacement of the top of the image is zero relative to the probe (the lateral displacement of the top of the image is not zero as tissue might slip under the probe). Therefore, we enforce the axial displacement of the first sample to be zero by changing the first row of D_1, ${I_2}'^{,2}$ and I'_2 . Fourth, we make the displacement estimation robust via IRLS using the Cauchy function (Equation 3.10). Similar to 1D AM, T is selected manually. For the first (seed) RF line, a small value can be selected for T if DP results are trusted. For the next lines, the value of Δd determines the accuracy of the Taylor expansion 14: for a small Δd, the residuals of the inliers are small and therefore a small T can be chosen, while for a large Δd the inliers might give large residuals and therefore a large value for T is required. Since the tissue motion is mostly continuous, Δd mostly depends on the lateral sampling of the image (i.e. the number of A-line per cm). Therefore, if many A-lines are given per cm of the image width, a small value of T will give the optimum results. Since the amplitude of signal is decreasing due to attenuation, we decrease the IRLS parameter T with depth by multiplying it with ζ_i at each sample i. With these modifications, Equation 3.10 becomes

$$(W{I'^2}_2 + ZD_1 + ZD_2)\Delta d = WI'_2 e - ZD_1 d + s \qquad (3.19)$$

Where W=diag(0,w(r_1),w(r_2),w(r_2)…w(r_m)w(r_m)) (i.e. $W_{2i,2i} = W_{2i-1,2i-1} =$ w(r_i) for i=1…m except for $W_{1,1} = 0$ which guarantees the displacement of the first sample to be zero) is the weight function determined by the residuals $r_i = I_1(i,j) - [I_2(i + d_{i,j} + a_i) + \Delta d_i I'_{2,z} + \Delta a_i I'_{2,x}]$, w is as before (Equation3.10), the bias term s is a vector of length 2m whose all elements are zero except the 2m-1thelement:s2m-1 = $\alpha\epsilon$, and $\epsilon = (d_m - d_1/m - 1)$ is as before. Similar to Equation 3.11, the coefficient matrix $Q = WI'^2_2 + ZD_1 + ZD_2$ is strictly diagonally dominant, symmetric and all the diagonal entries are positive. Therefore, Q is positive definite which means that solving Equation 3.14 results in the global minimum of the cost function C. The updated

displacement field (axial and lateral) will be $d + \Delta d$. Equation 3.14 can be solved for Δd in 9m operations since the coefficient matrix $WI_2'^2 + ZD_1 + ZD_2$ is pentadiagonal and symmetric. This number is again significantly less than $(2cm)^3/3$, the number of operations required to solve a full system.

3.1.1.3 Strain Estimation and Kalman Filter

Strain estimation requires spatial derivation of the displacement field. Since differentiation amplifies the signal noise, least squares regression (LSR) techniques are commonly used to obtain the strain field. Adjacent RF-lines are usually processed independently in strain calculation. However, the strain value of each pixel is not independent from the strain value of its neighboring pixels. The only exception is the boundary of two tissue types with different mechanical properties where the strain field is discontinuous. We use the prior of piecewise strain continuity via a Kalman filter to improve the quality of strain estimation.

We first calculate the strain using least squares regression. Each RF-line is first differentiated independently, for each sample i, a line is fitted to the displacement estimates in a window of length 2k + 1 around i, i.e. to the samples i - k to i + k. The slope of the line, $z_{i,j}$, is calculated as the strain measurement at i. The center of the window is then moved to i + 1 and the strain value $z_{i+1,j}$ is calculated. We reuse overlapping terms in calculation of $z_{i,j}$ and $z_{i+1,j}$, and therefore the running time is independent of the window length 2k+1. Having $z_{i,j}$ for i = 1…m and j = 1…n, we propose the following algorithm based on Kalman filter to take into account the prior of strain continuity.

$z_{i,j}$ j are the noisy measurements of the underlying strain field $\epsilon_{i,j}$. Since the $z_{i,j}$ values are calculated using axial windows, we apply the Kalman filter in the lateral direction. Let r_j be the Gaussian process noise and s_j be the Gaussian measurement noise to be removed. We have [38-39]

$$\epsilon_{i,j} = \epsilon_{i,j-1} + r_{i,j} \qquad (3.20)$$

$$z_{i,j} = \epsilon_{i,j} + s_{i,j} \qquad (3.21)$$

Let $\hat{\epsilon}^{-}_{i,j}$(note the super minus) be our a priori strain estimate from the process prior to step j (i.e. from the Equation 3.7) and $\hat{\epsilon}_{i,j}$ be our a posterior strain estimate at step j given measurement z_j . Let also the variances of $\hat{\epsilon}^{-}_{i,j}$and $\hat{\epsilon}_{i,j}$ be respectively $p^{-}$and p. The time update (i.e. prior estimation) equations will be [39]

$$\hat{\epsilon}^{-}_{i,j}=\hat{\epsilon}_{i,j-1} \qquad (3.22)$$

$$p^{-}_{i,j} = p_{i,j-1} + \sigma^2_r \qquad (3.23)$$

where σ^2_r is the variance of the process noise r. $p_{i,j-1}$ is initialized to zero for the first sample j = 1. The measurement update equations will be [42]

$$\hat{\epsilon}_{i,j}=\hat{\epsilon}^{-}_{i,j}+\frac{p^{-}_{i,j}}{p^{-}_{i,j}+\sigma^2_s}(z_{i,j}-\hat{\epsilon}^{-}_{i,j}) \qquad (3.24)$$

$$p_{i,j} = (1-\frac{p^{-}_{i,j}}{p^{-}_{i,j}+\sigma^2_s})p^{-}_{i,j} \qquad (3.25)$$

Where σ^2_s is the variance of the measurement noise s. Note that since both the state $\epsilon_{i,j}$and measurement $z_{i,j}$are scalars, all the update equations only require scalar operations. We estimate σ^2_r andσ^2_s as following. Let the mean (calculated using a Gaussian kernel of standard deviation of σ_G= 0.6 sample) of the strain values in 3×3 blocks around samples (i,j-1) and (i,j) be $\mu_{j-1}$and $\mu_j$respectively. Then σ^2_r is [43]

$$\sigma^2_r = (\mu_{j-1}-\mu_j)^2 \qquad (3.26)$$

This is a reasonable estimate of σ^2_r as it tries to capture the difference between pixel values at adjacent RF-lines. If the difference between the mean strain values is high, less weight is given to the a priori estimate. This space-variant estimation of the model noise provides a better match to local variations in the underlying tissue leading to a greater noise reduction. σ^2_s is the variance of$z_{i,j}$ measurements in the entire image and is constant throughout the image.

3.1.2 Segmentation

Segmentation is one of the most difficult tasks in image processing, segmentation using region growing was proposed on this work; As its name implies, region growing is a procedure that groups pixels or sub regions into larger regions based on predefined criteria for growth. The basic approach is to start with a set of "seed" points and from these grow regions by appending to each seed those neighboring pixels that have predefined properties similar to the seed (such as specific ranges of gray level or color). Selecting a set of one or more seed points often can be based on the nature of the problem, when a priori information is not available, one procedure is to compute at every pixel the same set of properties that ultimately will be used to assign pixels to regions during the growing process. If the result of these computations shows clusters of values, the pixels whose properties place them near the centroid of these clusters can be used as seeds. [44]

Selection of the seed of the seed pixel may be manual selection as done here or provided by an external algorithm. Whereas, the measure of similarity may be the absolute difference between the selected pixel and the neighborhood.

Region growing algorithm was found to be the best algorithm for the problem at hand; because of the phantom object is coherent and has similar intensity value, hence, it outputs better results than other algorithms as threshold and active contour.

3.1.3 Strain Ratio

Strain ratio is metric that determine the ratio of the lesion strain to the background strain, it’s dimensionless metric that specifies the measurement to which strain was applied to the object.

In the proposed work, the stain is calculated by taking a segment (a block) of the lesion where the strain was dominant namely the lower edge of the object, then it’s compared with a block of the same size to the background, all obtained from the same strain image. The ratio then was calculated from the average value of each block. And a single metric result was obtain quantifying the ratio. [21]

$$\text{Strain ratio} = \frac{\text{Lesion strain mean}}{\text{background strain mean}} \qquad (3.28)$$

3.1.4 Area and diameter calculations:

The area and diameter were calculated using Matlabs' built-in functions that infers them from the region properties. The area firstly calculated from the segmented object by counting the number of positively labeled pixels (pixels which have value of one) and then summing all those pixels. Diameter is then inferred from the area by calculating the range of pixel locations either in the X-axis or the Y-axis.

3.2 Material

Field II [45] and ABAQUS (Providence, RI) software are used for ultrasound simulation and for finite element simulation. Many scatterers are distributed in a volume and an ultrasound image is created by convolving all scatterers with the point spread function of the ultrasound and adding the results using superposition. The phantom is then meshed and compressed using finite element simulation, giving the 3D displacement of each node of the mesh. The displacement of each scatterer is then calculated by interpolating the displacement of its neighboring nodes. Scatterers are then moved accordingly and the second ultrasound image is generated. The displacement and strain fields are then calculated using the AM methods and are compared with the ground truth.

The parameters of the ultrasound probe are set to mimic commercial probes. The probe frequency is 7.27 MHz, the sampling rate is 40 MHz and the fractional andwidth is 60%. A Hanning window is used for apodization, the single transmit focus is at 22.5 mm, equi-distance receive foci are from 5 mm to 45 mm at each 5 mm, the transmit is sequential, and the number of active elements is 64. Two simulated phantoms are generated. The first phantom is $50 \times 10 \times 55$ mm and the second one is $36 \times 10 \times 25$ mm. Respectively 5×10^5 And 1.4×10^5 scatterers with Gaussian scattering strengths [46] are uniformly distributed in the

first and second phantom, ensuring more than 10 scatterers [47] exist in a resolution cell.

The mechanical properties of both phantoms, required for finite element simulation, is assumed to be isotropic and homogeneous. The first phantom is uniform while the second phantom contains a circular hole filled with blood that can move out-of-plane, simulating a blood vessel in tissue (Figure 3.2 (a)). The scatterers are distributed in the vessel, also with the same intensity and distribution as the surrounding material. A uniform compression in the z direction is applied and the 3D displacement field of phantoms is calculated using ABAQUS. The Poisson's ratio is set to $\nu = 0.49$ in both phantoms to mimic real tissue [33,48], which causes the phantoms to deform in x & y directions as a result of the compression in the z direction.

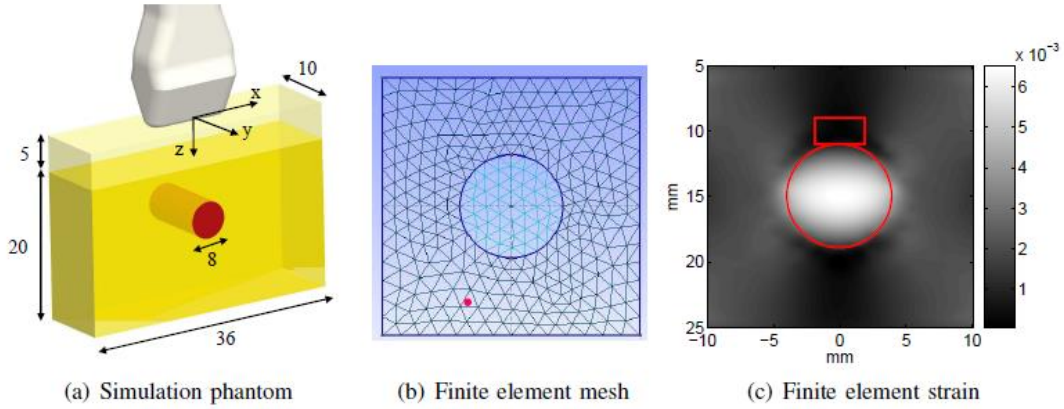

(a) Simulation phantom (b) Finite element mesh (c) Finite element strain

Fig 3.3 Second simulation experiment. Measurements in (a) are in mm. In (b), a scatterer is shown in the bottom left part as a red dot. Its displacement is calculated by interpolating the displacements of its 3 neighboring nodes on the mesh. (c) is the target (circular) and background (rectangular) windows. [29]

Chapter Four

Result and Discussion

4. Result and Discussion

For experimental evaluation, RF data is acquired from an Antares Siemens system (Issaquah, WA) at the center frequency of 6.67 MHz with a VF10-5 linear array at a sampling rate of 40 MHz The 2D AM method is used in the experimental results.

A breast elastography phantom (CIRS, Norfolk, VA) with a lesion of 10 mm diameter and three times stiffer than the background was palpated freehand.

The tunable parameters of the 2D AM algorithm are set to $\propto$ = 5, β_a= 10, β_l = 0:005 and T= 0.2, and the tunable parameters of the DP (run for the seed RF-line in the 2D AM algorithm) are α_a= α_l= 0.15 in all the phantom results (except if specified otherwise).

4.1 Phantom Result

An elastography phantom (CIRS elastography phantom, Norfolk, VA) was compressed 0.2 in axially using a linear stage, resulting in an average strain of 6%. And then two RF frames were obtained corresponding to before and after the compression. The Young's elasticity modulus of the background and the lesion under compression were respectively 33 kPa and 56 kPa.

4.1.1 Analytical minimization 2D

The displacement map was calculated using the 2D AM method. Figure 4.1 shows the axial and lateral displacement.

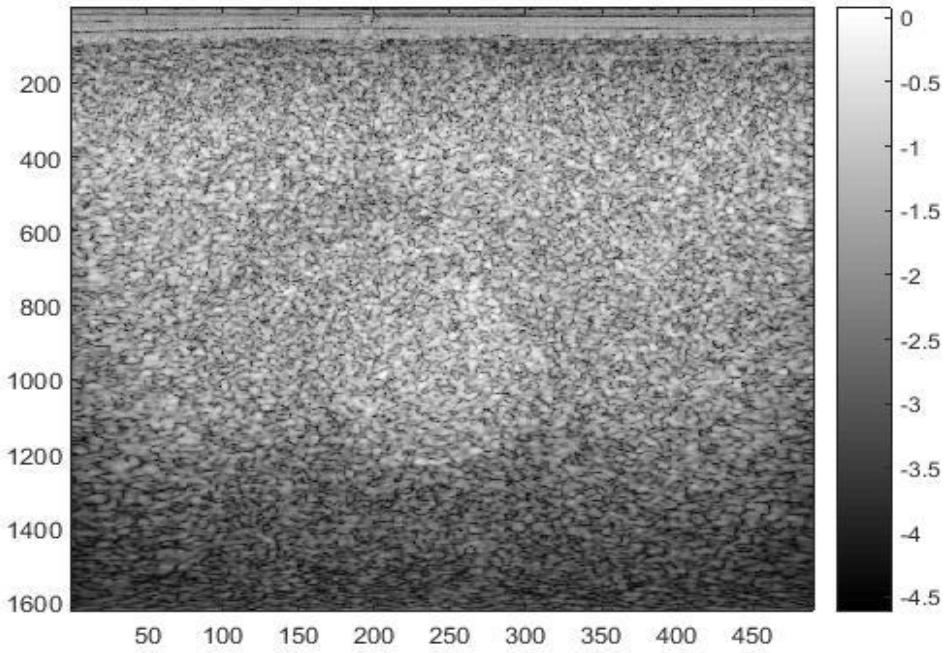

(a) Original image

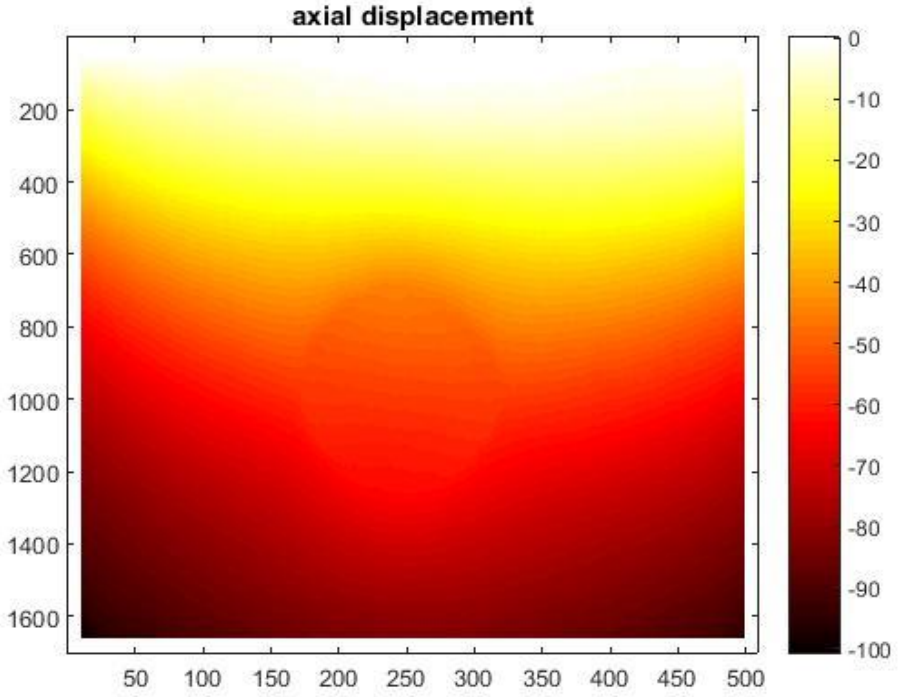

(b) Axial displacement (mm)

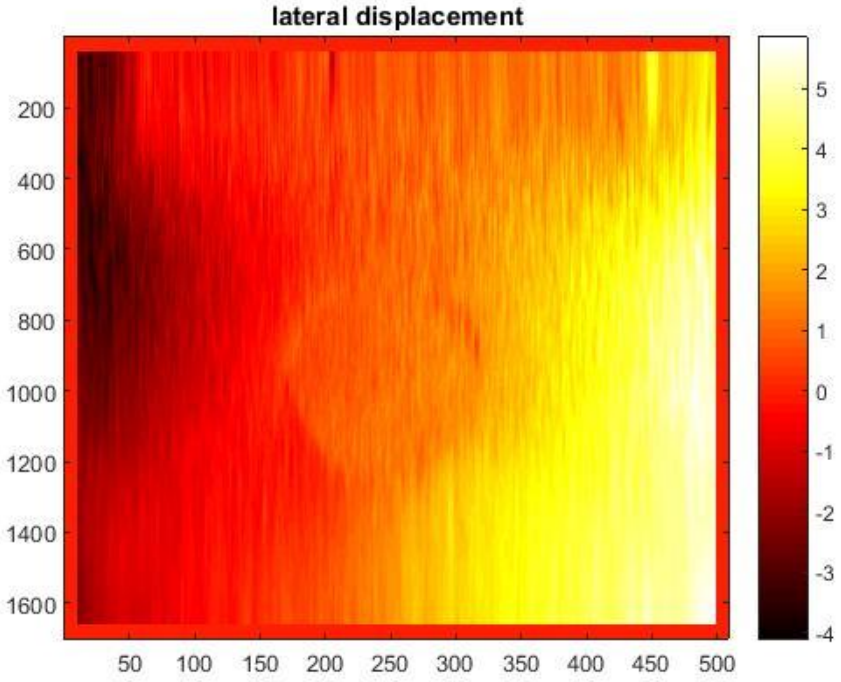

(c) Lateral displacement (mm)

Fig.4.1. Performance of the 2D analytical minimization (2D AM), (a) shows the original image, (b) is axial displacement in mm, and (c) is lateral displacement in mm.

In the previous figure the axial and lateral displacement were calculated to show movement of the tissue, that was used in strain calculation.

4.1.2 Least square regression and Kalman filter

The linear least squares differentiation technique was applied to the axial and lateral displacements field calculated with 2D AM, to obtained strain image (elastogram). Figure 4.2 shows the axial and lateral strain.

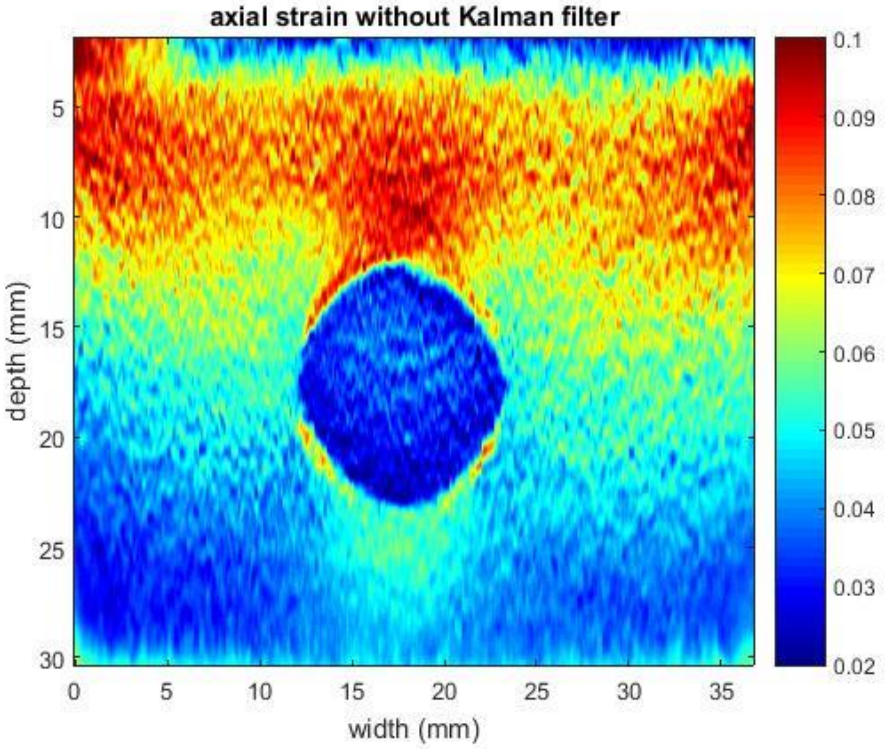

(a)Axial strain

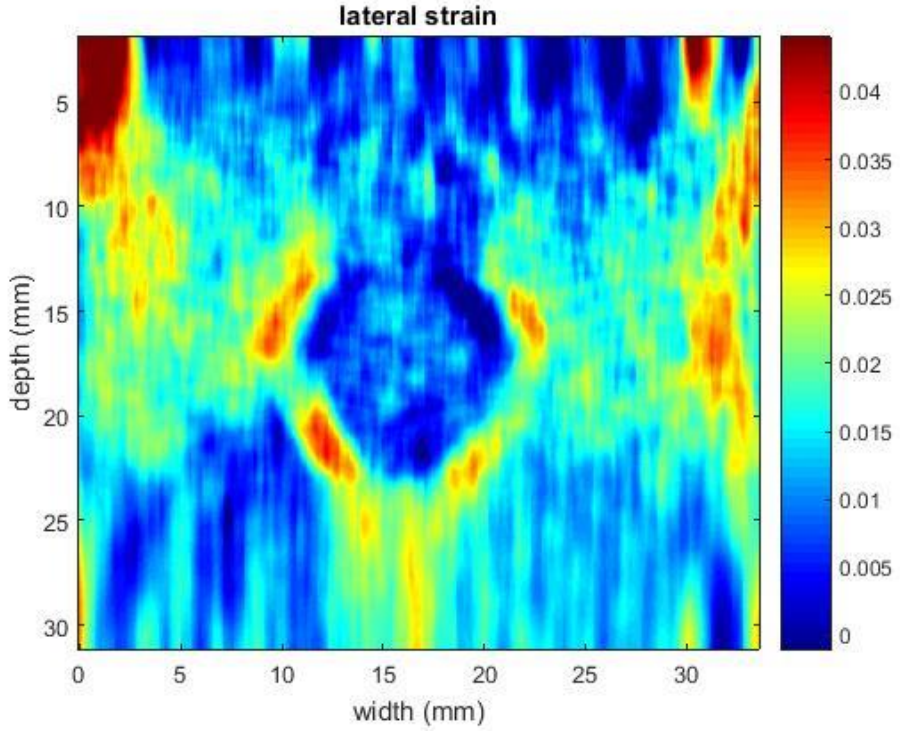

(b) lateral strain

Fig.4.2. Performance of the least squares regression in experimental data, (a) shows axial strain, while (b) is lateral strain.

In figure 4.2 comparing the strain values at a horizontal line of (a) and (b), the noisy $z_{i,j}$ measurements were smoothed in the lateral direction using the proposed least square regression, with minimal blurring of the edge.

The Kalman filter was then used to axial strain image. Figure 4.3 shows using of Kalman filter in denoising of axial image.

The pixels of images in (a) and (b) were respectively the least squares measurements. The Kalman filter removes the noise while keeping the image sharp, due to the variable model noise.

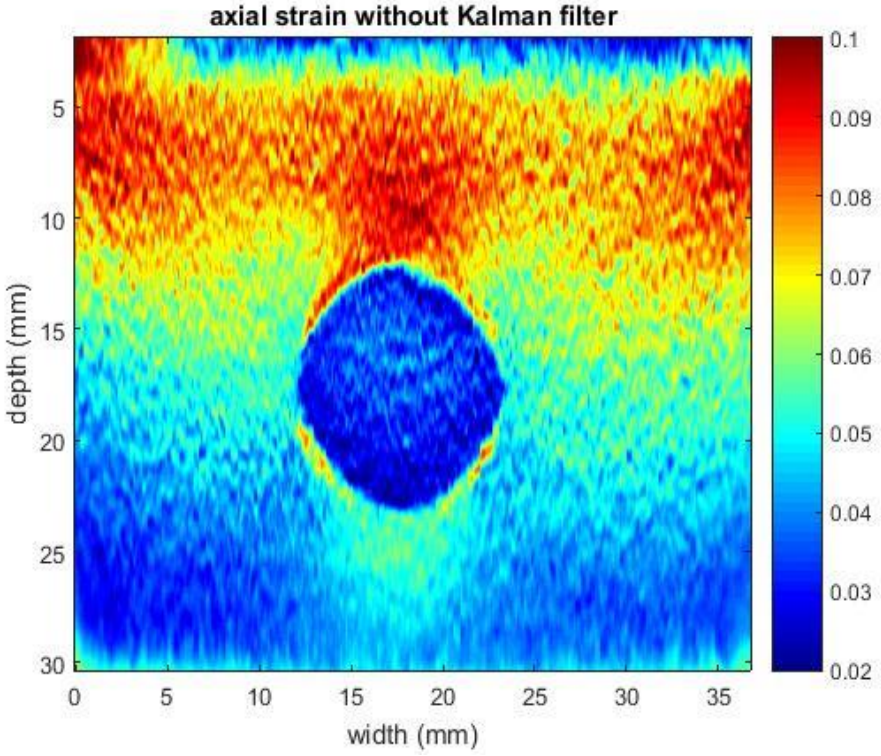

(a) Strain without KF

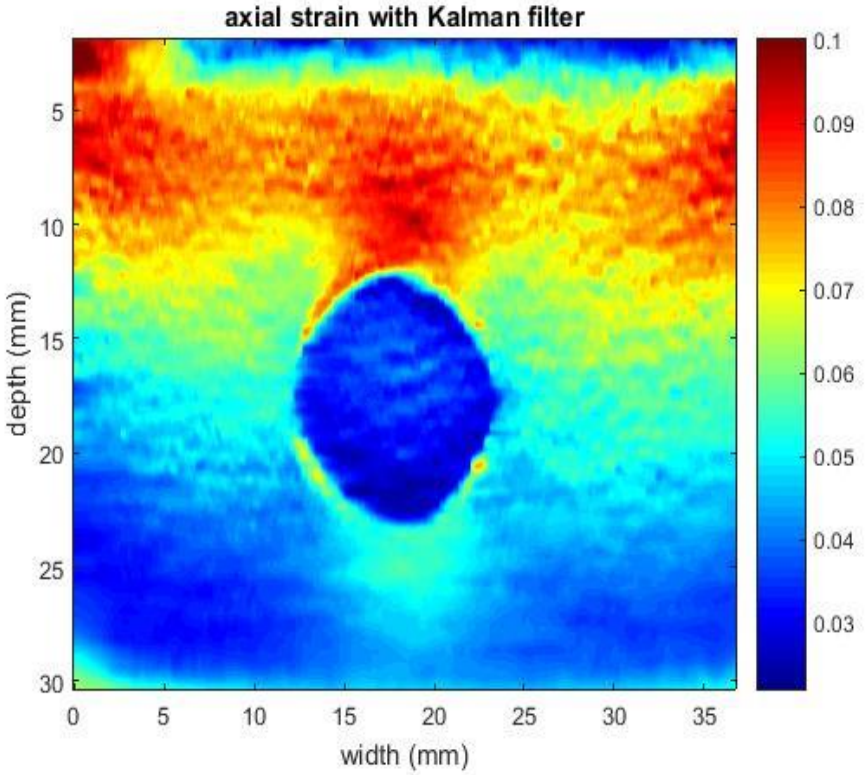

(b) strain with KF

Fig.4.3. performance of Kalman filter in experimental data. (a) shows the axial strain field calculated by least squares regression of the noisy displacement field. (b) depicts the strain field calculated from the noisy measurements of (a) (KF in (a) and (b) refers to Kalman filter).

4.1.3. Region growing segmentation

Image segmentation was optimal way to extract object from the background. Three different types of image segmentation were used (active contour, threshold, and region growing), region growing gave beast result that properly segmentped the object from back ground comparing it with active contour and threshold.

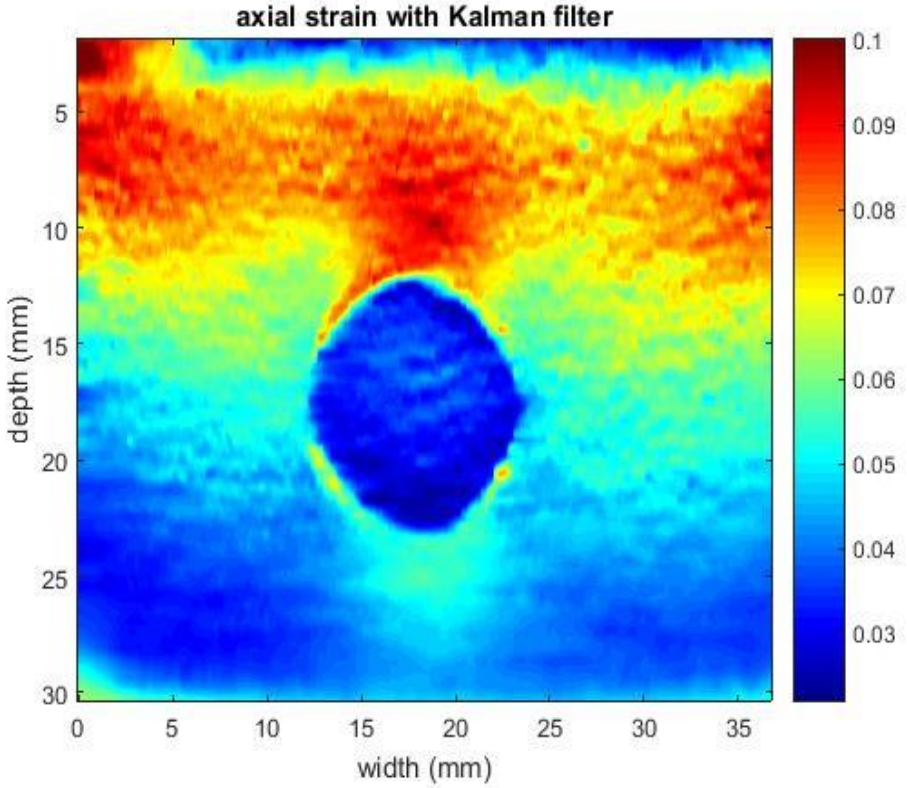

(a) Image Before Segmentation

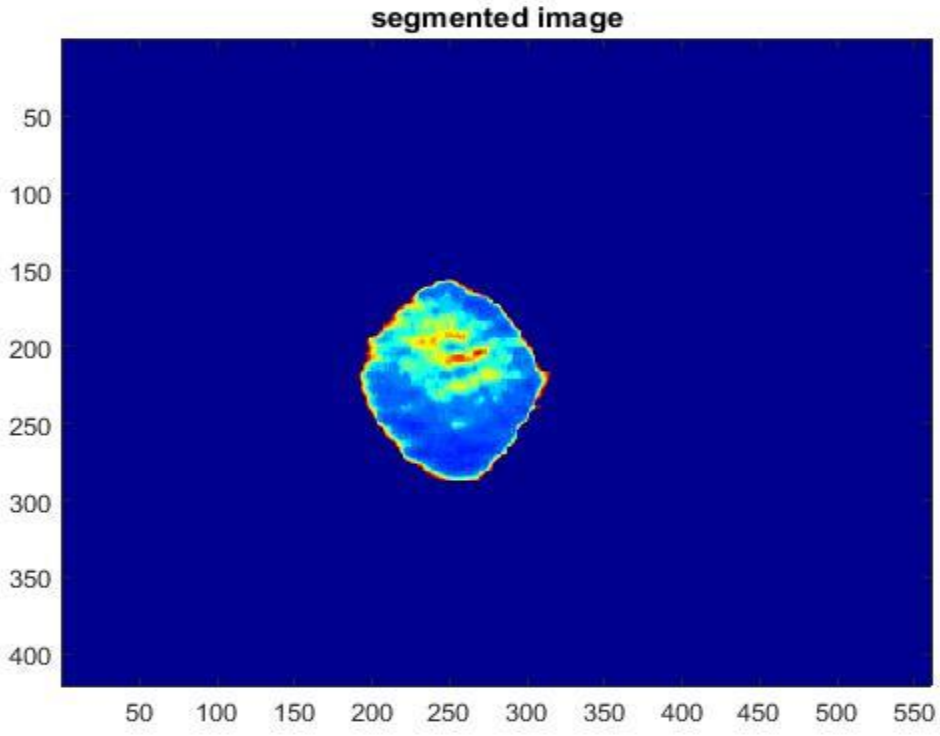

(b) image After Segmentation

Fig 4.4 Performance of region growing segmentation, (a) represent the image *before segmentation, and in (b) the object is segmented from the background.

Segmentation was used to segment the object from the back ground, to calculate the strain ratio and the diameter and area.

4.1.4. Strain ratio

The strain ratio was calculated to determine the lesion stiffness that is use in classification between tissue types; the result of calculation shows that the strain ratio was 0.4; which indicates that the lesion has 0.4 strain ratio less than background strain, which may indicate there is a potential abnormality exist in the lesion area.

The diameter and area were calculated to be compared with the given data for the phantom to assess the accuracy of the result obtained by the quantitative elastography. The diameter was 11.5644 mm and the phantom lesion diameter was 12 mm and the area was 195.9429 mm^2, compared to 196 mm^2 with the phantoms' result; which means that the calculation result are accurate compared with the phantoms' results.

Chapter Five

Conclusion and Recommendation

5.1 Conclusion

Qualitative elastography alone did not give information about tissue stiffness, so in this thesis quantitative elastography was proposed to determine the lesion stiffness. In the quantitative elastography the suspicion lesion was automatically been segmented from the background. And then the strain ratio of the lesion was calculated to show the lesion stiffness, diameter and area were also measured to calculate dimensions of the lesion. The strain ratio gives information about lesion stiffness, so it can be used for further tumor classification.

From all above it could be concluded that:

- Segmentation using region growing algorithm performed with best result compared with k-means and active contours.
- The strain ratio was 0.4; which means the lesion has 0.4 strain ratio less than background strain, which may indicate there is a potential abnormality exist in the lesion area.
- Calculations of the diameter, area, and strain ratio shown very close results to the phantom result which means that the implementation is quite accurate and yields to reliable results.

5.2 Recommendation

The following recommendations are suggested:

Formerly quantitative elastography can be used for real data (patient) instead of phantom.

Finally, the value of strain ratio can be used in classification between tumor types and grades.

Reference

[1] V. Asha, Kim Upadhyay. Ultrasound Elastography- Implication in the Head and Neck region. International Journal of Scientific Study Case Reports & Reviews, 2014; 3(1).

[2] Satyanand Tyagi, Sachin Kumar. Clinical Applications of Elastography: An Overview. International Journal of Pharma and Bio Sciences, 2010; 3(1).

[3] Ophir J, Caspedes I, Ponnekanti H, et al. Elastography: a quantitative method for imaging the elasticity of biological tissue. Ultrason Imaging, 1991; 13(2): 111-134.

[4] Krouskop TA, Wheeler TM, Kallel F, et al. Elastic moduli of breast and prostate tissues under compression. Ultrason Imaging, 1998; 20: 260-274.

[5] Ophir J, Alam SK, Garra B, et al. Elastography: ultrasonic estimation and imaging of the elastic properties of tissues. Proc Inst Mech Eng H, 1999; 213: 203-233.

[6] Garra, BS. Imaging and estimation of tissue elasticity by ultrasound. Ultrasound Q, 2007; 23: 255-268.

[7] Debdutta Das1, Monika Gupta1, Harkamal Kaur1, Aman Kalucha. Elastography: the next step. Journal of Oral Science, 2011; 53(2): 137-141.

[8] Urszula Zaleska-Dorobisz et al. Ultrasound Elastography- Review of Techniques and its Clinical Applications. Adv Clin Exp Med, 2014; 23(4): 645–655.

[9] Cosgrove D. et al. EFSUMB Guidelines and Reccomendations on the Clinical Use of Ultrasound Elastography. Part 2: Clinical Application, 2013.

[10] Itoh A Et al. Clinical application of US elastography for diagnosis. Radiology, 2006; 239(2): 341-350.

[11] Sarvazyan A et al. An overview of elastography – an emerging branch of medical imaging. Curr Med Imaging Rev, 2011; 30(4): 429-436.

[12] Aguilo MA et al. An inverse problem approach for elasticity imaging through vibroacoustics. Medical Imaging, IEEE Transactions, 2010; 29(4): 1012-1021.

[13] Armen Sarvazyan et al. An Overview of Elastography- An Emerging Branch of Medical Imaging. Current Medical iImaging Reviews, 2011; 7(4): 255-282.

[14] Bamber J. EFSUMB guidelines and recommendations on the clinical use of Ultrasound Elastography. Part 1: Basic Principles and Technology; Ultraschall Med, 2013.

[15] Szabo TL. Diagnostic ultrasound imaging: inside out. Academic Press; 2004.

[16] Parker KJ et al. A unified view of imaging the elastic properties of tissue. The Journal of the Acoustical Society of America, 2005; 117(5): 2705-2712.

[17] Young Jun Choi et al. Ultrasound Elastography for Evaluation of Cervical Lymph Nodes. Ultrasonography, 2015; 34(3): 157-164.

[18] Dighe M, Bae U, Richardson ML, Dubinsky TH, Minoshima S, Kim Y. Differential Diagnosis of Thyroid Nodules with US Elastography Using Carotid Artery Pulsation. Radiol. 2008; 248:662-669.

[19] RAJ, Jean Rossario; RAHMAN, Syed Mohammed Khalilur; ANAND, Sneh. Preliminary evaluation of differentiation of benign and malignant breast tumors using non-invasive diagnostic modalities. Biomedical Research, 2016.

[20] Gong, X., Wang, Y. and Wu, W., 2016. Value of ultrasound elastography in diagnosis of BI-RADS 4B breast lesions based on conventional ultrasound. INTERNATIONAL JOURNAL OF CLINICAL AND EXPERIMENTAL MEDICINE, 9(2), pp.2561-2566.

[21] Stoian, D., Timar, B., Craina, M., Bernad, E., Petre, I. and Craciunescu, M., 2016. Qualitative strain elastography–strain ratio evaluation-an important tool in breast cancer diagnostic. Medical ultrasonography, 18(2), pp.195-200.

[22] Cheng KL, Choi YJ, Shim WH, Lee JH, Baek JH. Virtual touch tissue imaging quantification shear wave elastography: prospective assessment of cervical lymph nodes. Ultrasound in Medicine and Biology. 2016 Feb 1;42(2):378-86.

[23] Wahba AA, Khalifa NM, Seddik AF, El-Adawy MI. A finite element model for recognizing breast cancer. Journal of Biomedical Science and Engineering. 2014 Apr 1;7(05):296.

[24] Ramalli A, Bassi L, Boni E, Ricci S, Giannotti E, Abdulcadir D, Nori J, Tortoli P. Real-time implementation of a novel algorithm for ultrasound freehand elastography of breast lesions. InAcoustics, Speech and Signal Processing (ICASSP), 2014 IEEE International Conference on 2014 May 4 (pp. 5158-5161). IEEE.

[25] Liu XJ, Zhu Y, Liu PF, Xu YL. Elastography for breast cancer diagnosis: a useful tool for small and BI-RADS 4 lesions. Asian Pac J Cancer Prev. 2014 Jan 1;15(24):10739-43.

[26] Olgun DÇ, Korkmazer B, Kılıç F, Dikici AS, Velidedeoğlu M, Aydoğan F, Kantarcı F, Yılmaz MH. Use of shear wave elastography to differentiate benign and malignant breast lesions. Diagnostic and Interventional Radiology. 2014 May;20(3):239.

[27] Coelho B. Ultrasound Elastography: Prostate Cancer Detection Assessment Using a Phantom. Journal of ultrasound. 2013 Jan 1;15(13):981.

[28] Fiorini E, Cipriano V, De Molo C, Righi S, Ainora ME, Arcelli A, Bertusi C, Montanari M, Bianchi G, Serra C. Real-time elastography as a noninvasive technique for quantification of fibrosis in patients with chronic viral liver disease: preliminary findings. Journal of ultrasound. 2012 Dec 1;15(4):220-5.

[29] Rivaz H, Boctor EM, Choti MA, Hager GD. Real-time regularized ultrasound elastography. IEEE transactions on medical imaging. 2011 Apr;30(4):928-45.

[30] Chiorean A, Duma MM, Dudea SM, Iancu A, Dumitriu D, Roman R, Sfrangeu S. Real-time ultrasound elastography of the breast: state of the art. Medical Ultrasonography. 2008 Dec 1;10(2):73-82.

[31] Rivaz H, Boctor E, Foroughi P, Zellars R, Fichtinger G, Hager G. Ultrasound elastography: a dynamic programming approach. IEEE transactions on medical imaging. 2008 Oct;27(10):1373-7.

[32] Pellot-Barakat C, Sridhar M, Lindfors KK, Insana MF. Ultrasonic elasticity imaging as a tool for breast cancer diagnosis and research. Current Medical Imaging Reviews. 2006 Feb 1;2(1):157-64.

[33] Rivaz H, Boctor EM, Fichtinger G. P3E-9 ultrasound speckle detection using low order moments. InUltrasonics Symposium, 2006. IEEE 2006 Oct 2 (pp. 2092-2095). IEEE.

[34] Bertsimas D, Tsitsiklis J. Biomechanics: Mechanical Properties of Living Tissues.

[35] Huber PJ. Robust statistics Wiley 308p.

[36] Hager GD, Belhumeur PN. Efficient region tracking with parametric models of geometry and illumination. IEEE transactions on pattern analysis and machine intelligence. 1998 Oct;20(10):1025-39.

[37] Holland PW, Welsch RE. Robust regression using iteratively reweighted least-squares. Communications in Statistics-theory and Methods. 1977 Jan 1;6(9):813-27.

[38] E. Konofagou and J. Ophir, “A new elastographic method for estimation and imaging of lateral displacements, lateral strains, corrected axial strains and

poisson's ratios in tissues," Ultrasound Med. and Biol., vol. 24, no. 8, pp. 1183–1199, 1998.

[39] Sandrin L, Tanter M, Catheline S, Fink M. Shear modulus imaging with 2-D transient elastography. IEEE transactions on ultrasonics, ferroelectrics, and frequency control. 2002 Apr;49(4):426-35.

[40] Tanter M, Bercoff J, Sandrin L, Fink M. Ultrafast compound imaging for 2-D motion vector estimation: Application to transient elastography. IEEE transactions on ultrasonics, ferroelectrics, and frequency control. 2002 Oct;49(10):1363-74.

[41] Chen L, Treece GM, Lindop JE, Gee AH, Prager RW. A quality-guided displacement tracking algorithm for ultrasonic elasticity imaging. Medical image analysis. 2009 Apr 1;13(2):286-96.

[42] Prince JL, Links JM. Medical imaging signals and systems. Upper Saddle River: Pearson Prentice Hall; 2006.

[43] Krouskop TA, Wheeler TM, Kallel F, Garra BS, Hall T. Elastic moduli of breast and prostate tissues under compression. Ultrasonic imaging. 1998 Oct;20(4):260-74.

[44] Gonzalez Rafael C, Woods Richard E, Eddins Steven L. Digital image processing using MATLAB. Editorial Pearson-Prentice Hall. USA. 2004.

[45] Jensen JA. Field: A program for simulating ultrasound systems. In10TH NORDICBALTIC CONFERENCE ON BIOMEDICAL IMAGING, VOL. 4, SUPPLEMENT 1, PART 1: 351--353 1996.

[46] Wagner RF. Statistics of speckle in ultrasound B-scans. IEEE Trans. Sonics & Ultrason. 1983;30(3):156-63.

[47] Rivaz H, Boctor EM, Fichtinger G. P3E-9 ultrasound speckle detection using low order moments. InUltrasonics Symposium, 2006. IEEE 2006 Oct 2 (pp. 2092-2095). IEEE.

[48] Krouskop TA, Wheeler TM, Kallel F, Garra BS, Hall T. Elastic moduli of breast and prostate tissues under compression. Ultrasonic imaging. 1998 Oct;20(4):260-74.